UNIVERSITAT POLITÈCNICA DE VALÈNCIA

Escuela Técnica Superior de Ingeniería del Diseño

UNIVERSITAT POLITÈCNICA DE VALÈNCIA

School of Design Engineering

CFD-based study of hydrogen injection in swirling aeronautic combustion chambers

Master's Thesis

Master's Degree in Computational Fluid Dynamics

AUTHOR: Burgo Beiro, Marcos

Tutor: Martí Gómez-Aldaraví, Pedro

ACADEMIC YEAR: 2023/2024

UNIVERSITAT POLITÈCNICA DE VALÈNCIA

Escuela Técnica Superior de Ingeniería del Diseño

Master Thesis

CFD-based study of hydrogen injection in swirling aeronautic combustion chambers

Author:

Marcos Burgo Beiro

Supervisor:

Pedro Martí Gómez-Aldaraví

Master's degree in Computational Fluid Dynamics
Escuela Técnica Superior de Ingeniería del Diseño
Universitat Politècnica de València

València - March 2024

Abstract

As environmental regulations tighten their grip on the mobility industry, the pursuit of cleaner alternatives, particularly hydrogen combustion, gains momentum. Aeronautical engines, known for their demanding operational conditions, present a formidable engineering challenge in transitioning to sustainable energy sources. This thesis utilizes Computational Fluid Dynamics, specifically with the CONVERGE software, to examine the cold-flow dynamics of hydrogen-fueled aeronautical combustion chambers using Reynolds-Averaged Navier-Stokes (RANS) and Large Eddy Simulation (LES) approaches. A key finding highlights the malfunctioning of swirl-inducing devices in specific operating conditions, crucial for enhancing combustion chamber performance. Significantly, the RANS approach proves inadequate in capturing higher-frequency oscillations induced by these "swirlers" within turbulent structures, revealing a trade-off between increased computational cost and simulation reliability. This research delves into the challenges and opportunities associated with adopting hydrogen combustion in aeronautical engines, addressing the nuanced complexities of sustainable propulsion systems in this context.

Contents

List of Figures

List of Tables

Nomenclature

Symbols

λ	air-fuel equivalence ratio
ϕ	fuel-air equivalence ratio
κ	Turbulent kinetic energy
ϵ	Turbulent dissipation rate
Fr	Froude Number
Re	Reynolds Number
Ma	Mach Number

Abbreviations

AMR Adaptative Mesh Refinement

CFD Computational Fluid Dynamics

CFL Courant-Friedrich-Lewy number

CRZ Corner Recirculation Zone

DNS Direct Numerical Simulation

FFT Fast Fourier Transform

GTF Geared Turbo Fan

IRZ Inner Recirculation Zone

LES Large Eddy Simulation

MQA Mesh Quality Assesment

RANS Reynolds-Averaged Navier-Stokes

SAF Sustainable Aviation Fuel

SGS Sub-Grid Scale

SOR Successive Over Relaxation

1. Introduction

1.1. Justification and objectives

The downfall of fossil fuels as an energy source is nowadays a reality that almost every industrial sector must face and adapt to, especially in the European Union. Both in power generation and transport applications, technologies are in constant evolution to seek, in some cases better performances of well-known systems, and in other cases brand-new ideas that can entirely transform our conceptions of some operating mechanisms.

The aerospace industry is not an exception to these changes, in fact, it is responsible for 13 % of the total transport CO_2 emissions in the European Union which are expected to be reduced by 90 % in 2050 (compared to 1990 logs) [11]. With this purpose, many different paths drift apart in the approach to the solution for this problem. Huge companies in the aerospace field such as *General Electric* are developing in parallel some very revolutionary concepts like hybrid-electric propulsion systems, the *OpenFan* program, new compact engine core designs, or the use of alternative fuels, such as SAF or hydrogen [18]. *Pratt & Whitney* and *Rolls Royce*, other two main engine manufacturers, highlight the crucial importance of investing in research to design engines that generate less pollutant emissions, developing the *GTF* and *Ultrafan* concepts respectively [27] [28].

Hydrogen, either used in a fuel cell to power electric motors or burnt in the combustion chamber of an engine, is one of the so-called "hot topics" in industrial research all around the globe [36] [19]. The main advantage of hydrogen combustion over regular gasoline or diesel combustion is that, while these propellants generate CO_2, CO, and NO_x particles, hydrogen combustion, when reacting with pure oxygen, only generates water vapor.

Many vehicle manufacturers have been testing prototypes running on hydrogen-powered internal combustion engines for ground vehicles [22] [35]. However, it is well-known that aeronautic engines represent complicated systems and are restricted to rigid regulations that can cause a slowdown of the process. In spite of this, one of the two most powerful aircraft manufacturers in the world, *Airbus*, has recurrently declared its compromise with hydrogen combustion technologies all over the past years [1]. *Airbus*, as some other of the leading engineering companies, is a member of the *hydrogen Council*, which is a global initiative of 132 leading energy, transport, industry, and investment companies with a united and long-term vision to develop the hydrogen economy who also pursue the benefits of cross-industry experience [8].

Once the importance of hydrogen combustion in aeronautic engines is evidenced, the aim of this project is to study a particular type of combustion chamber and the phenomena occurring inside it. These phenomena are evaluated both independently and in their effect on the system's overall behavior.

1. The so-called swirlers are structures that have been designed to introduce a radial velocity component and therefore enhance the oxidizer-propellant mixture. One of the aims of this project is to analyze their performance and how they affect or not the flow depending on the injection conditions.

2. To identify the turbulent structures that are generated inside the combustion chamber and be able to relate them to the quality of the mixing.

3. To study the influence of injection composition in the mixture process, as well as in the behavior of the flow inside the combustion chamber. Analyze this data together with the theory about hydrogen combustion to define the most desired operating conditions for the engine.

4. To define which of these phenomena can be studied using the results from the RANS turbulence approach and which remains hidden when all the turbulence in the domain is modeled and therefore must be studied using methods such as LES or even DNS.

This project was developed using *Converge* CFD software, at the facilities of CMT-Motores Térmicos in Valéncia.

1.2. Aeronautic engines

Jet engines have had a huge impact on mobility since being introduced more than half a century ago. Particularly, turbofan engines have evolved to match the wide variety of operating conditions, ranges, and environmental regulations they have been exposed to in civil and military aviation. In this kind of engine, the primary flow is compressed in a number of compressor stages each one formed by a rotor and a stator, then gets driven into the combustion chamber where the fuel is injected and the reaction occurs to provide energy to the air passing through it, and once out of the combustion chamber it goes through a set of turbine stages which extract some of that energy from the flow to power the compressor stages, meanwhile, the secondary or bypass flow gets accelerated by the fan, being the main contributor of the total thrust. By moving a large amount of air at relatively low speeds, the modern turbofan engines, also known as "high bypass ratio" engines, raise their efficiency over the traditional turbofan engines, with a lower bypass ratio [17].

Weight and size are both major concerns when designing an aircraft, as the more over-dimensioned all the parts in the aircraft are, the worse it will perform in fuel waste per unit transported. The mixing process studied in this project is especially relevant to this objective for two main reasons:

- The swirling injection into the combustion chamber is intended to make the flow develop in all three directions in space, achieving a more homogeneous concentration distribution. This can help to reduce the required length of the combustion chamber and consequently allowing the engine to be more compact and less heavy.

- A correct mixing also prevents abnormal combustion (this topic will be explained in detail in the next section), hence reducing the amount of after-treatment that the exhaust gases will need before being taken out to the atmosphere.

For this reason, most jet engines mounted have some kind of technology to reduce the length of the combustion chamber, such as reverse-flow combustion chambers or multiple annular combustion chambers [32].

1.3. Hydrogen combustion

Although this project does not directly model the combustion process, it is crucial to understand the mechanism of hydrogen combustion to be able to correctly build the numerical model and extract the relevant information from its results.

Hydrogen has a relevant advantage over traditional fuels, it allows a much wider range of flammability taking into account the richness of the mixture. The air-fuel equivalence ratio (defined in Equation 1.1) that the air-hydrogen mixture can handle ranges from as lean as $\lambda = 10$ to as rich as $\lambda = 0.14$ [36].

$$\lambda = \frac{\text{air-fuel ratio}}{\text{air-fuel ratio}_{stechiometric}} \tag{1.1}$$

$$\phi = \frac{\text{fuel-to-oxidizer ratio}}{\text{fuel-to-oxidizer ratio}_{stechiometric}} \tag{1.2}$$

These characteristics encourage the experimentation of a wide range of strategies, most aiming to maximize output power while minimizing pollutant emissions. It is important to highlight that, despite the hydrogen combustion process itself does not create any kind of harmful emissions (1.3), the problem comes with NO_x emissions that are created as a side effect. The air that is injected inside the combustion chamber comes from the atmosphere and is mostly composed of nitrogen (78 %) and oxygen (21 %) [24]. Oxygen is necessary for the combustion process but at temperatures as high as the ones reached in a jet engine combustion chamber, the excess oxygen found in lean mixtures reacts with nitrogen and forms different NO_x products (1.4), mainly NO, this process is known as "thermal NO" or "Zeldovich mechanism" and it occurs in fuel-air mixed flames [20]. Below around 750^{o}C, virtually no NO is formed [19]. These kinds of pollutant emissions are predominantly controlled by peak and average flame temperatures, so this underlines the importance of the mixing process, which, if performed correctly, can slow down the combustion process and reduce these issues [7].

$$2H_2 + O_2 \rightarrow 2H_2O \tag{1.3}$$

$$\begin{aligned} N_2 + O &\rightarrow NO + N \\ N + O_2 &\rightarrow NO + O \\ N + OH &\rightarrow NO + H \end{aligned} \tag{1.4}$$

In general, a lean combustion regime is desirable so the excess air in lean operation acts as an inert gas and effectively reduces combustion temperatures and consequently component temperatures. This significantly reduces the occurrence of abnormal combustion in lean combustion regimes [36].

Although different conditions are tested in this project, none of them belong to the auto-ignition zone of the hydrogen [38], represented in Figure 1.1, where all the different conditions will be at the top-left part of the graph, below the auto-ignition crossover for any fuel-air equivalence ratio (defined in Equation 1.2), so the choice of not modeling combustion and focusing on the fuel-air mixture does not necessarily imply unphysical assumptions despite being a study of just "part of the problem".

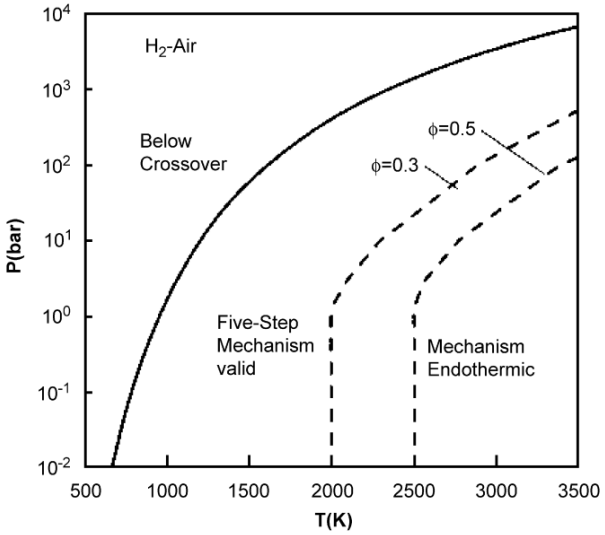

Figure 1.1: Auto-ignition zones for hydrogen-air mixture (extracted from [38])

1.4. State of the art

This project is an independent, self-standing work, however, one particular previous investigation has been taken as a reference for some reference values and procedures [3]. This study aims to provide a deeper comprehension of the phenomena controlling ignition and flame propagation as occurring in real combustors using CFD. Also, the other purpose of this work is the assessment of LES models to provide a reliable numerical methodology to achieve an ignition sequence in real engines. It is composed of a series of cold-flow simulations that aim to validate the simulation setup for the following steps, where the combustion modeling is included in the case, and both single-injector and multiple-injector variations of the geometry are tested and compared to experimental data.

Despite the geometry of the problem is not completely equal, this work was taken as a reference to build both the post-processing measurements, and the boundary conditions at the inlet of the domain. Also, by the time this thesis is being written, the ongoing project lacks experimental data, so the cited thesis is taken as a reference frame on the behavior of the cold-flow simulations.

Due to the large presence of hydrogen combustion everywhere nowadays, a large number of projects are being developed at the moment and have been consulting to give this work a greater picture when talking about aeronautic combustion chambers running on hydrogen CFD modeling ([10], [25]). But other projects are being developed approaching the performance of these systems in other ares, such as noise generation ([23]).

2. Numercial setup

2.1. Geometry

The geometry is composed, on its first part, of two different ducts. These two ducts flow separately up to the point where the seven swirlers are located for the outer duct, from this point on, both ducts mix in a single cylindrical tube up to the combustion chamber. The combustion chamber has a length (Y dimension) of 260 mm with a square section of 100 mm. The actual device is located at the facilities of *CMT - Clean Mobility and Thermofluids* in València and can be observed in Figure 2.1.

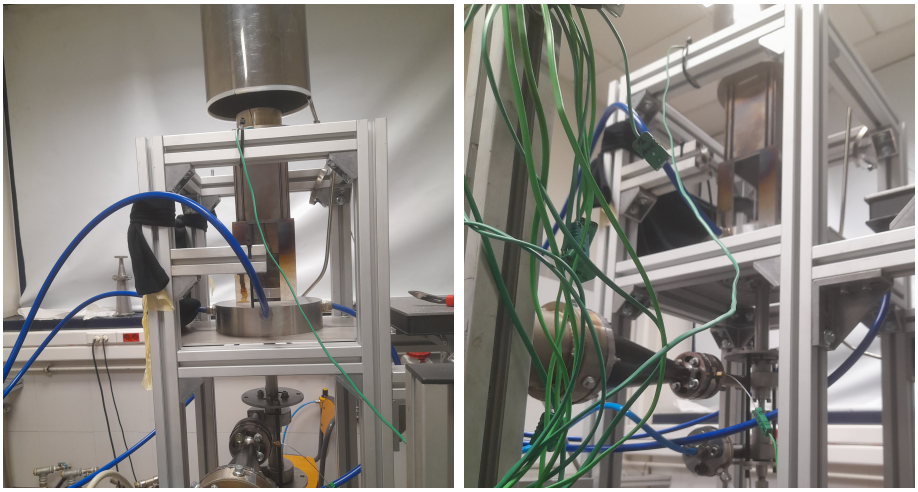

Figure 2.1: Experimental burner

From the actual burner geometry, a CAD model was obtained and cleaned up, so it is prepared to introduce it to a CFD software (see Figure 2.2). The geometry was separated into different parts, distinguishing both inlets, the outlet, and the walls which are sub-split depending on their orientation and the region they belong to. The purpose of this separation is to facilitate the pre and postprocessing operations and be able to individually fix any topology problem that could come up.

The distance from the swirler location up to the inlet of the combustion chamber and the number and shape of swirlers are two very important parameters whose modification could mean a significant change in the behavior of the system. In spite of that, these modifications are outside the scope of this project and therefore will be fixed.

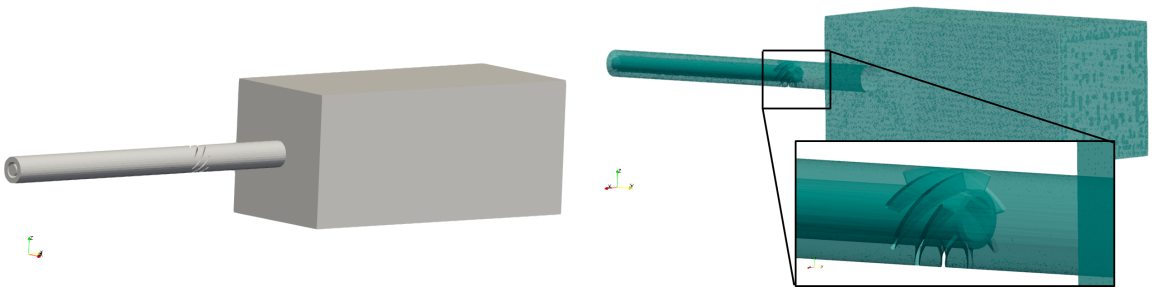

Figure 2.2: Geometry domain and swirler detail

In order to make the pre-processing stage simpler, the geometry has been divided into three different regions, named inlet region, mixing region, and combustion chamber, and identified with colors green, orange, and red respectively in 2.3 this will allow to the application of some tools to large groups of boundaries in an easy way.

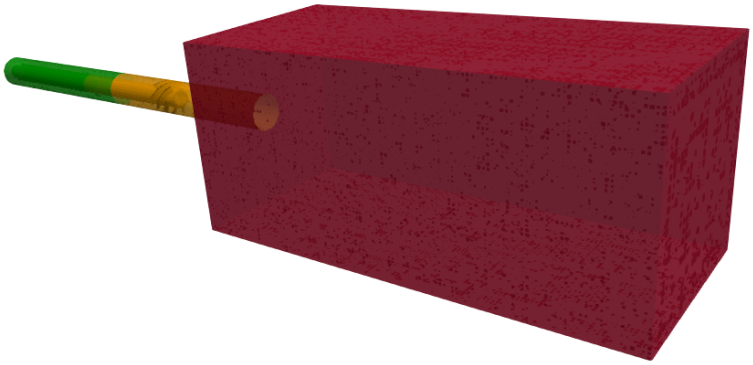

Figure 2.3: Region definition divided in colors

2.2. Multiphase modeling

As the fluid that flows through the domain is not composed of a single gas, but of three different ones, the model must account for this in some manner. This study runs an Euler-Euler approach, as Oxygen, Nitrogen, and Hydrogen are miscible gases.

The mixture model for multiphase flows is attained by adding the phase conservation equations together, so instead of solving one equation for each phase, it solves one set of equations for the mixture, where the material properties (density, viscosity, and thermal conductivity) of the mixture are evaluated as the weighted average of the different phases (Equation 2.1). This stands also for the pressure field, which is assumed to be shared among all phases. The mixture velocity and enthalpy are defined as stated in Equation 2.2, where N is the number of phases, k is the phase index, α stands for the volumetric fraction and the "m" index stands for the mixture.

$$\rho^m = \sum_{k=1}^{N} \alpha_k \cdot \rho_k \ ; \ \mu^m = \sum_{k=1}^{N} \alpha_k \cdot \mu_k \ ; \ \kappa^m = \sum_{k=1}^{N} \alpha_k \cdot \kappa_k \tag{2.1}$$

$$\rho_m u_m = \sum_{k=1}^{N} \alpha_k \rho_k u_k \ ; \ \rho_m h_m = \sum_{k=1}^{N} \alpha_k \rho_k h_k \tag{2.2}$$

The mixture model allows the phases to have different velocities, introducing a drift velocity (Equation 2.3) (difference between a phase velocity and the mixture velocity) and slip velocity (velocity difference between two phases). However, a more simplified model can be used if the difference in velocity between phases is neglected, this is the homogeneous model, which is not used in this project.

$$u_k^{drift} = u_k - u_m \tag{2.3}$$

Taking into account the previous assumptions, the Reynolds-averaged form of transport equations results as stated in Equations 2.5 (mass conservation), 2.6 (momentum conservation), and 2.7 (energy conservation). Note that gravity forces are not represented in the equations,

this is because through dimensional analysis using the Froude Number (defined in 2.4, where u is a characteristic velocity, L_0 a characteristic length and g stands for the value of gravitational acceleration), it becomes clear the gravity forces are several orders of magnitude below the inertial forces ($Fr \approx 10^2$ for the worst case scenario). In the equations below, the term F_{sigma} refers to the sum of the forces acting in the interface, while the term ζ stands for the product of those forces times the interface velocity.

$$Fr = \frac{u^2}{gL_0} \tag{2.4}$$

$$\frac{\partial \rho_m}{\partial t} + \nabla(\rho_m \mathbf{u}_m) = 0 \tag{2.5}$$

$$\begin{aligned} &\frac{\partial \left(\rho^m \mathbf{u}^m\right)}{\partial t} + \nabla \cdot \left(\rho^m \mathbf{u}^m \times \mathbf{u}^m\right) = -\nabla p + \nabla \cdot \left\{\mu^m \left[\nabla \mathbf{u}^m + \left(\nabla \mathbf{u}^m\right)^T\right] - \frac{2}{3}\mu^m \nabla \cdot \mathbf{u}^m \delta\right\} \\ &- \nabla \cdot \tau^{m''} + \mathbf{F}_\sigma - \nabla \cdot \sum_{k=1}^{N} \left(\alpha^k \rho^k \mathbf{u}^{dr,k} \times \mathbf{u}^{dr,k}\right) \end{aligned} \tag{2.6}$$

$$\frac{\partial \left(\rho^m H^m\right)}{\partial t} + \nabla \cdot \left(\rho^m \mathbf{u}^m H^m\right) = \nabla \cdot \left(\kappa^m \nabla T^m\right) + \zeta - \sum_{k=1}^{N} \left(\alpha^k \rho^k \mathbf{u}^{dr,k} H^k\right) \tag{2.7}$$

These equations will suffer some more changes when using the turbulent viscosity assumption, as well as the turbulence model equations must also be modified to take into account the various phases that coexist in the domain, but this will be treated in a further section (2.5).

The mixture model is still unclosed because of the introduction of N new variables by using the volumetric fractions of all the species. This is solved using N-1 equations like Equation 2.8, which physically stands for the phase change and reaction mechanisms that can turn one phase into another. For the last N specie, it is imposed the condition that the sum of all volume fractions must be equal to 1 (2.9).

$$\frac{\partial \left(\alpha^k \rho^k\right)}{\partial t} + \nabla \cdot \left(\alpha^k \rho^k \mathbf{u}^k\right) = \sum_{l=1}^{N} \left(\dot{m}_{lk} - \dot{m}_{kl}\right) \tag{2.8}$$

$$\sum_{k=1}^{N} \alpha^k = 1 \tag{2.9}$$

The mixture model is a widely used multiphase model, its main advantages over other models are its simplicity and its computational efficiency [31].

2.3. Time treatment

The time treatment is a sensible topic when working with high velocities as in this case. A transient approach is used in this case, as the injection of the air-hydrogen mixture is evaluated in this project, also, this allows to study the stabilization process of the flow in the combustion chamber. With this intention, the case is simulated for 0.05 s, this time corresponds to 25 times the residence time for the worst-case scenario in terms of mean flow axial velocity, this has been considered to be enough to capture this stabilization process.

The time step will be controlled by the variable time-step algorithm available in *Converge*. This algorithm performs a number of checks and then takes the largest time-step that satisfies

all of the applicable limiters [30]. The relevant ones for this specific case are exposed in Table 2.1.

$$CFL = u \cdot \frac{\Delta t}{\Delta x} \leq 1 \tag{2.10}$$

Time-step limiter	Formulation	Explanation
dt_grow	$dt \leq 1.25 \cdot dt_{prev}$	Every cycle, *Converge* attempts to increase the time-step by 25%
dt_max	$dt \leq dt_{max}$	User-defined maximum time-step
dt_min	$dt \geq dt_{min}$	User-defined minimum time-step
dt_cfl	$max\_cfl\_u \geq u\frac{\Delta t}{\Delta x}$	Convection CFL
dt_piso	$dt \leq 0.75 \cdot dt_{prev}$	Reduces the timestep if the PISO iterations were larger than a predefined maximum

Table 2.1: Time-step limiters

The *Converge* interface allows the user to see which is the limiting condition in each time-step. Continuously reaching one or both of the user-defined explicit limits (dt_{max} or dt_{min}) may indicate that those limits are not well defined.

Keeping the CFL number (defined in 2.10) under 1, physically means that the information will, at most, travel the distance equivalent to a cell size at each time-step. This condition guarantees stability for explicit schemes [9]. Also, the temporal parameters are adjusted to avoid recurring iterations where the *PISO* algorithm reaches its maximum number of iterations without meeting the convergence criteria. A summary of the time parameters used in this setup is exposed in 2.2.

Variable	Value	Units
Start time	0	s
End time	0.05	s
Initial time-step	10^{-6}	s
Maximum time-step	10^{-5}	s
Minimum time-step	10^{-7}	s
Maximum Convection CFL limit	1	-

Table 2.2: Summary of time paramters

2.4. Spatial discretisation

When using *Converge* CFD software, the grid is automatically generated at runtime, this differs from many other programs where the meshing process is separated from the solving process. *Converge* uses a modified cut-cell cartesian grid generation method. In short, this type of algorithm immerses the geometry in a cartesian block and then trims the cells at the intersection surface. To avoid poor-quality cells, the algorithm also searches for cut-cells whose volume is less than 30 % of the adjacent regular cell, if this happens, the cut-cell and the regular cell are paired into a single node. This process is called cell-pairing. Too much cell pairing along one direction can lead to the formation of slender cells with a high aspect ratio, which occurs most frequently along the boundaries where the geometry is sharp and the grid size is too coarse. Too many cells with a high aspect ratio can lead to numerical dispersion errors

and a less robust simulation so it is important to be sensible to the geometry sharpness when defining the cell size for a specific zone.

The mesh generation process was approached firstly intending to do a mesh independence analysis while selecting a mesh that was refined in the regions where the hydrogen-air mix was expected to carry a higher velocity (namely inlet and mixing regions), this would lead to higher gradients and therefore a fine mesh would be needed to capture those gradients. Then uniform variations to the named mesh would be done, leading to the non-dependence of a group of testing parameters on the mesh size, also known as mesh independence. However, the size of the mesh required to make this work was proven to exceed the amount of resources assigned to this part of the project, so this idea was rejected.

The next step taken in order to achieve a functioning mesh was to use the AMR. The main idea behind AMR is to automatically refine the grid on regions where there are high gradients of variables such as velocity or temperature, avoiding the calculations to be slowed down by a much more heavy globally refined grid. *Converge* includes two types of AMR refining, but in this case, the SGS field AMR is preferred. This aims to embed the mesh in the under-resolved parts of the flow field. The sub-grid field is defined as the difference between the resolved field and the actual field, it is calculated using the expression in Equation 2.11, where ϕ' is the subgrid-scale scalar. A cell is embedded if the absolute value of the sub-grid field is above a user-specified value. Conversely, a cell is released if the absolute value of the subgrid is below 1/5 of the user-specified value.

$$\phi' \approx -\alpha_k \frac{\partial^2 \bar{\phi}}{\partial x_k \partial x_k} \tag{2.11}$$

This second meshing approach also includes an embedding near the walls of the geometry, which is necessary as the velocity in those places is not enough to force an embedding through AMR and it is necessary to keep the Y+ value in the desired range.

The difference between the two meshing approaches is illustrated in Figure 2.4, where two of the meshes used in the iterative process are exposed. In terms of cell number, both meshes are different but the point is that they have comparable cell sizes. In the first mesh, the mixing region has been embedded but the transition to the combustion chamber may be too fast and the mesh ends up not having enough resolution in the space where vortex breakdown occurs, it also has an excessively small mesh size in the end part of the combustion chamber, where gradients are low and it is outside the interest of the analysis. On the other hand, the AMR mesh refines the zone where velocity profiles are important and therefore will catch more accurately the vortex breakdown processes, leaving the back and the corners of the combustion chamber unrefined, computational resources are saved.

Of course, AMR has a computational cost associated with the calculations of the SGS field and the mesh changes, but in this case, it is considered to be worth it because of the impossibility of correctly meshing the vortex breakdown phenomena. More information about the meshing process and the mesh quality assessment procedures can be found in Section 3.

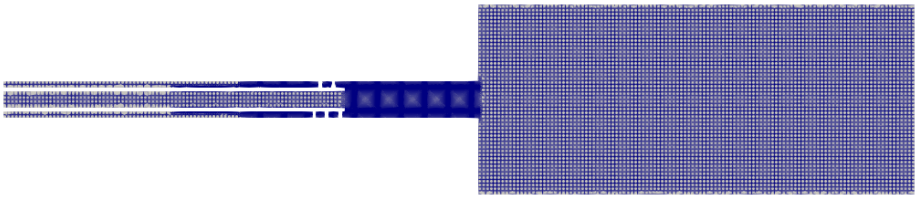

904609 cells, without AMR

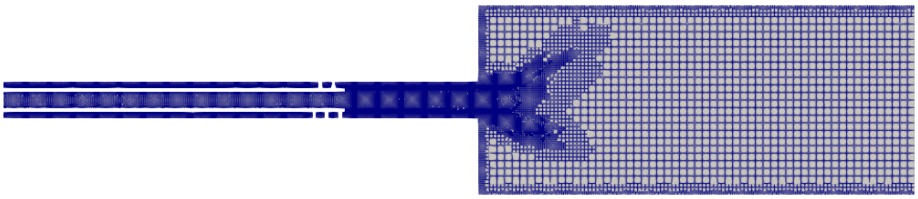

1552503 cells, with AMR

Figure 2.4: Meshing approaches comparison

2.5. Turbulence modeling

Turbulence is known to be present in flows whose Reynolds numbers are above a certain threshold (normally around $Re = 4000$ [26] for internal flows), turbulent flows are defined by some common characteristics:

- Irregularity: velocity varies significantly in space and time
- Three-dimensional vorticity fluctuations.
- Dissipation

Since the complexity of these flows exceeds the current computation capabilities, those irregularities must be modeled using statistical methods, namely, in the development of this project RANS and LES approaches were used.

2.5.1 RANS

In RANS, the equations are solved for the average velocity field, when doing this averaging an unknown term rises, this term is called the Reynolds stress and is determined by a turbulence model. In the present work, a turbulent viscosity model is used, namely the $\kappa - \epsilon$ model, which solves a transport equation bot for the turbulent kinetic energy (2.12) and the turbulent

dissipation rate (Equation 2.13), whose parameters represent a compromise to cover a wide range of simple applications (Table 2.3), therefore it is classified as a two-equation model. $\kappa-\epsilon$ model is arguably the most famous turbulence model and is implemented in nearly every CFD multi-use code.

$$\frac{\partial \rho k}{\partial t} + \frac{\partial \rho u_i k}{\partial x_i} = \tau_{ij}\frac{\partial u_i}{\partial x_j} + \frac{\partial}{\partial x_j}\frac{\mu + \mu_t}{Pr_k}\frac{\partial k}{\partial x_j} - \rho\varepsilon + \frac{C_s}{1.5}S_s \tag{2.12}$$

$$\rho\frac{D\varepsilon}{Dt} = \frac{\varepsilon}{k}C_1 P + C_1'\rho v_t\frac{\varepsilon}{k}(\nabla\cdot u)^2 - C_{2n}\rho\frac{\varepsilon^2}{k} - \rho R_\varepsilon + C_3\rho\varepsilon(\nabla\cdot u) \tag{2.13}$$

Parameter	**Value**
C_1	1.42
C_μ	0.0845
η_0	4.38
β	0.012
b_0	2.0725
b_1	-0.3865
b_2	0.083

Table 2.3: Consat values for the $\kappa-\epsilon$ model

Particularly, from the wide variety of sub-models that have been developed over time, this work will be approached using $\kappa-\epsilon$ RNG model, which was developed using Re-Normalization Group methods in order to account for smaller scales of motion [39]. The main reason behind the choice of this model is that is called to be more accurate when simulating rotating cavities like the burner.

Since the $\kappa-\epsilon$ models are known for poorly predicting near-wall behavior [15], the boundary layer will be not solved but modeled using wall laws (Explained further in the next section). Because of this fact, the adimensional height of the first cell next to the wall must be big enough so the cell center is in the logarithmic region of the boundary layer ($30 < y^+ < 300$ [26])

2.5.2 LES

The LES turbulence modeling approach employs a different method to deal with flow variations. Turbulent flows are formed by eddies, which can have a wide range of sizes from the biggest scale in a particular problem, which is frequently named the turbulent scale, to the smallest ones, characterized by the Kolmogorov scale. This wide range of scales is represented in the energy cascade Figure 2.5, where the kinetic energy density is plotted against the wavenumber, which only depends on the diameter of the eddie and should not be misunderstood as equal to the turbulent kinetic energy, despite being also denoted by letter κ (Equation 2.14).

$$\kappa = \frac{2\pi}{d} \tag{2.14}$$

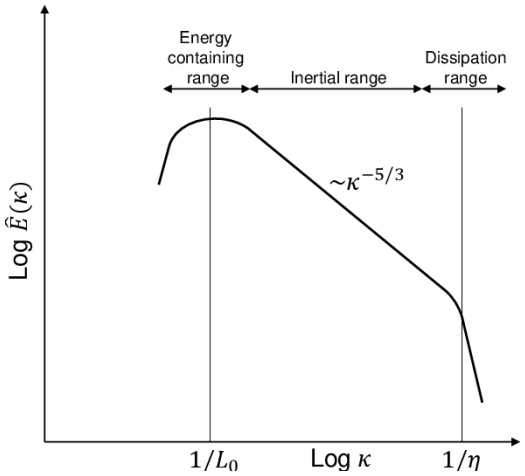

Figure 2.5: Turbulence energy cascade (Extracted from [16])

The point of an LES simulation is to resolve the majority (usually the lower threshold is set to 80 %) of the turbulent kinetic energy and model the rest, which is contained in the smallest, energy-dissipating eddies and is usually referred to as SGS. The main issue when using this kind of approach is that in order to properly capture an eddie of size d, as for the finite volumes method that is used in the CFD code the flow velocity is only calculated at the center of each cell, it would be needed at least 4 square cells of length $d/2$. This leads to a very small cell size which eventually leads to a high demand for computational resources.

The smallest eddies can not be resolved directly, so, just as in the RANS approach, a turbulence model is needed. This model must access the smallest solved eddies and model their shrink into smaller and smaller until they dissipate into heat, this is done by numerically raising the viscosity so these eddies are actually able to break up so the viscosity becomes $\nu = \nu + \nu_{sgs}$. For this purpose, an integral sub-grid scale is needed, which is an average of the existing scales but below the mesh size threshold. As this size must be smaller than the cell, it can be presented as the cell size times a coefficient (Equation 2.15).

$$l_{sgs} = C_s \cdot (CellVolume)^{\frac{1}{3}} \tag{2.15}$$

This coefficient must be obviously always below 1 , and with the use of this approach comes the assumption that eddies are isotropic, and have all the same shape, that is why their size can be characterized using only one variable.

Just as in RANS cases, in the subgrid model, the Reynolds stress tensor is the unknown variable for this problem. In order to close this problem the Dynamic Smagorinsky model is used, which uses the previously defined constant to calculate the sub-grid scale viscosity and belongs to zero-equation models. While the standard Smagorinsky model requires a user-input value for C_s, the dynamic model calculates it for every zone in the domain, being more accurate [13], coefficients were left to the default values recommended by *Converge* development team.

Regarding the flow near the wall, the Werner and Wengle model was used, which is a quite cheap model in terms of computational power while showing acceptable results. The model essentially imposes a linear and a log-law profile in the boundary layer‘s viscous and log-law subregions, respectively while avoiding specifying an equation for the buffer layer (Equation 2.16 , [37])

$$u^+ = \begin{cases} z^+ & for\ z^+ \leq 11.81 \\ A(z^+)^B for\ z^+ > 11.81 \end{cases} \quad Being\ A = 8.3\ and\ B = 1.7 \tag{2.16}$$

2.6. Solver Parameters

PISO algorithm was chosen as well as a density-based Navier-Stokes solver type, as this should be the most suitable setup for a transient compressible simulation. Also, a summary of the solvers used for each equation besides the parameters for them can be checked in the table 2.4:

Equation	Solver Type	Tolerance	Max iterations	SOR Relaxation
Momentum	SOR	$1e-05$	50	1.0
Pressure	SOR	$1e-08$	500	1.1
Density	SOR	$1e-04$	2	1.0
Energy	SOR	$1e-04$	2	1.0
Species	SOR	$1e-04$	2	1.0
$\boldsymbol{\kappa}$ (Only in RANS)	SOR	$1e-03$	50	0.7
$\boldsymbol{\epsilon}$ (Only in RANS)	SOR	$1e-03$	50	0.7

Table 2.4: PISO parameter definition

2.7. Initial and Boundary conditions

2.7.1 Boundary conditions

The geometry was divided into a total of 17 boundaries in order to have the capacity to impose special conditions if needed, however, for the whole development of this project, there were used only three different types of boundary conditions from the available ones when using *Converge* CFD code.

All the solid walls were split into 14 boundaries, but essentially were imposed the same conditions, selecting a *wall* type boundary condition. When no movement of the wall is prescribed (stationary wall), this type of boundary condition applies a Dirichlet boundary condition for the velocity, also known as a no-slip condition. Nevertheless, as for high-Reynolds numbers, it may not be possible to resolve the viscous sublayer of the flow, there is a special *law-of-wall* condition. The *law-of-the-wall* is a logarithmic curve fit of a turbulent boundary layer. In practice, the law-of-the-wall profile determines the tangential components of the stress tensor at the wall. Wall roughness is outside the scope of his project, so the roughness parameters are set to zero for the roughness height (K_s) and 0.5 for the roughness constant (C_s), despite the first value should be enough for the solver to not consider any roughness on the wall.

The geometry also is formed of two inlet surfaces, which will be named outer inlet and inner inlet from now on. The *inflow* boundary condition from the solver allows the modeling of these inlets. While the mass fractions of the components injected in them will be changed from one simulation to another in order to determine their influence on the combustion chamber state, the rest of the variables will be maintained throughout the course of the project and will be identical for both inlets except for the mass flow, the turbulent kinetic energy (κ) intensity and the turbulent dissipation (ϵ) length scale. The first values are directly extracted from [3], while the other are obtained from the following correlations shown in Equations 2.18 and 2.19, where d_h is the hydraulic diameter, and Re_dh is the Reynolds number based on it. Regarding mass flow, the code allows to directly impose the desired mass flow value as a special type of boundary condition and then internally calculates the velocity using Equation 2.17, where u is the resulting velocity, ρ_{ave} is the average density at the boundary, A is the total area of the boundary and n_i is the outward pointing normal of the boundary.

$$u_i = \frac{massflow}{\rho_{ave} \cdot A} \cdot n_i \tag{2.17}$$

$$I = 0.16 \cdot Re_{d_h}^{-1/8} \tag{2.18}$$

$$l = 0.038 \cdot d_h \tag{2.19}$$

Finally, the end part of the combustion chamber is set as an *outflow* boundary condition, which is essentially the same as an *inflow*, but in this case a Dirichlet boundary condition for the pressure, which is set at atmospheric pressure 101325 Pa, and a Neumann boundary condition for velocity, making it dependent from the declared pressure.

It is important to declare that the cold-flow simulations developed at this project do not account for heat transfer through the walls of the burner, so the temperature is set at 300 K as a Dirichlet boundary condition, and the walls are set as adiabatic, this is expressed with a Neumann boundary condition with the temperature gradient equal to zero. The definition of Dirichlet and Neumann boundary conditions can be consulted in Section 5.2

Boundary	**Variable**	**Condition Type**	**Value**
Inner	Velocity	Mass flow	0.000236
inlet	Pressure	Neumann	0
Outer	Velocity	Mass flow	0.005612
inlet	Pressure	Neumann	0
Outlet	Velocity	Neumann	0
	Pressure	Dirichlet	101325
Wall	Velocity	Dirichlet	0
	Pressure	Neumann	0

Table 2.5: Boundary conditions summary

2.7.2 Initial conditions

The initialization of variables in *Converge* CFD code is done using *Regions*, which can be consulted at 2.3. Even if the domain was split into three different regions, the initial conditions are identical for all three of them, the properties are displayed in Table 2.6. The fact that the domain initially contains only air, and not a mixture of air and H_2, means that the transient simulation will take more time to develop into an equilibrium solution but the lack of data regarding that initial concentration forces it to be done this way.

Variable	**Value**	**Units**
Velocity	[0,0,0]	m/s
Pressure	101325	Pa
Temperature	300	K
H_2 **Volume Fraction**	0	-
O_2 **Volume Fraction**	0.233	-
N_2 **Volume Fraction**	0.767	-
$\boldsymbol{\kappa}$	1	m^2/s^2
$\boldsymbol{\epsilon}$	100	m^2/s^3

Table 2.6: Initial conditions summary

3. Mesh Quality Assesment

3.1. RANS

As stated in previous chapters, the mesh approach was changed once the results of the first meshing setup were unable to provide a reasonable trade-off between the accuracy of results and the computational resources available.

3.1.1 No AMR-based meshing

This first part of this mesh quality assessment comprises a series of simulations where some minor overall scaling changes to the mesh were done. The parameters modified on this part of the project, are the base grid size and also the embeddings on the different flow regions (2.3), so the zones in the domain where higher gradients were expected, had a finer mesh size. Embeddings are calculated as follows in *CONVERGE*:

$$embedded\_grid = base\_grid/2^{embeddedscale} \tag{3.1}$$

In Table 3.1 the mesh variables for each test case are displayed, also, in Figure 3.1 all four meshes are displayed, ordered from left to right and from above to below, so changes between them can be visually appreciated.

Case	Base size [m]	Embedding zone(s)	Embedding scale	# cells
1 (a)	[0.003 , 0.003 , 0.003]	Reg 1	2	386855
2 (b)	[0.002 , 0.002 , 0.002]	Reg 1	2	904609
3 (c)	[0.003 , 0.003 , 0.003]	Reg 0 and Reg 1	2	531148
4 (d)	[0.004 , 0.004 , 0.004]	Reg 0 and Reg 1	3	2052023

Table 3.1: Mesh Parameter Summary

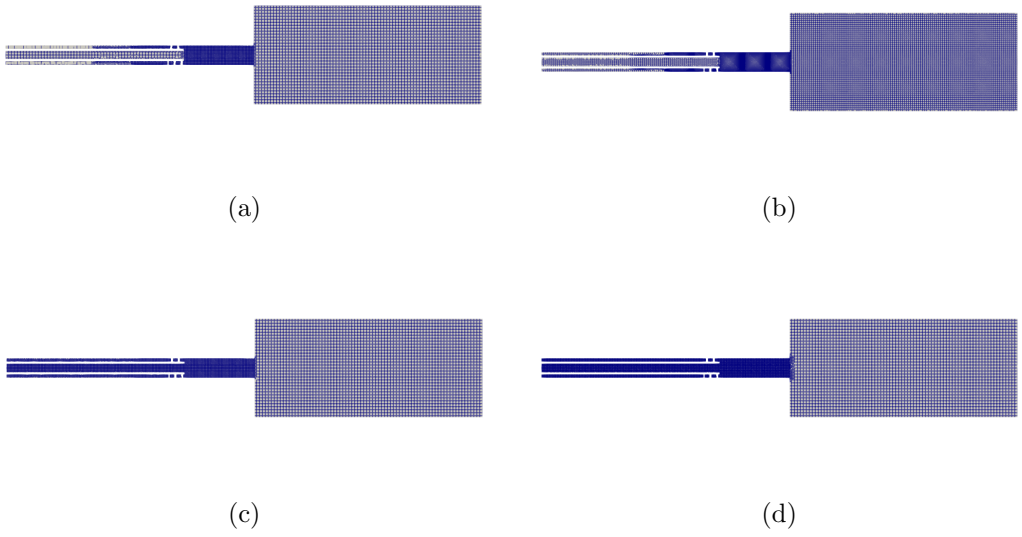

(a) (b)

(c) (d)

Figure 3.1: Side slice of the four tested meshes

For the mesh convergence analysis, both a global variable and a local one were used to measure the differences between the different meshes. The global variable chosen was the mass flow at the inlet of the combustion chamber. the value of this variable was equal for the four meshes at every recorded time-step, with a tolerance of 10^{-6} $[kgm^2/s]$, these results also guarantee the convergence of the case, as the conservation of mass flow rate is satisfied. Moving onto the local variable measured, the chosen parameter was velocity at the entrance of the combustion chamber (Point 1 on Figure 3.2)

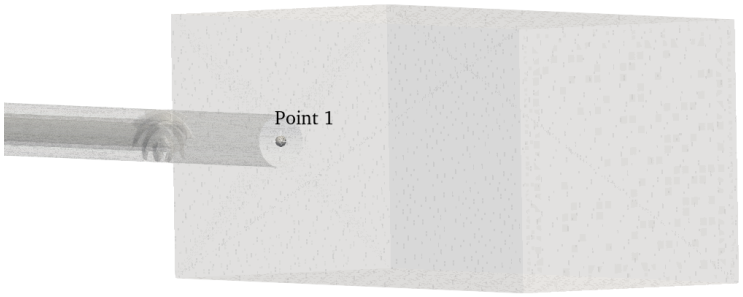

Figure 3.2: Point 1 Location

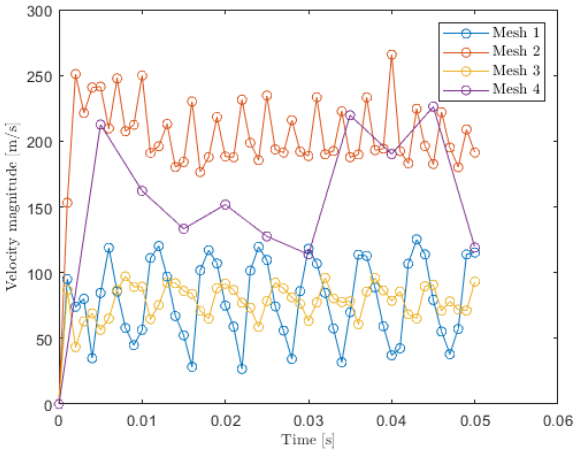

Figure 3.3: Velocity evolution for different meshes in point 1

As seen in Figure 3.3, the differences between the different meshing approaches do not follow any pattern, and the number of cells of each mesh does not correlate with the velocity at those points. This is because the vortex breakdown phenomena that are occurring at the entrance of the combustion chamber (Region 2) are not captured as the mesh is at its base grid size which is not fine enough. Refining the grid for the whole combustion chamber zone would be a waste of resources as the majority of it has a velocity inferior to 10 m/s, and using a refine-by-solid command using a cylinder or a rectangle would be difficult as the vortex breakdown zone, which will be addressed later, does not have a fixed width or length and therefore it will be over-refining the mesh at some timesteps and under-refining it on other ones. The solution for this meshing problem is to activate AMR meshing, which was already explained in Section 2.4.

Except for the species fraction, all the boundary conditions are defined for the whole project (see Table 2.5). For the mesh sensitivity analysis for RANS, the injection of both inflows is 100 % hydrogen, as for a given mass flow rate, the hydrogen´s smaller density leads to higher velocities, which are the worst-case scenario for the project setup.

3.1.2 AMR-based meshing

So as to conduct some tests on AMR meshing sensitivity, the mesh over which the AMR will act must be chosen before, in this case, the mesh was configured as stated in Table 3.2, being a relatively coarse mesh with refinements in the wall in order to keep the Y^+ inside the desired range for the wall functions to behave properly (between 30 and 300 approximately [30][29]), regarding this topic, note that the combustion chamber walls are the only boundaries flagged as a wall which do not belong to the high-velocity tube, hence, the embedding at this boundary will be of scale two instead of three, all the other parameters for the combustion chamber walls are identical to the other walls´ parameters. Figure 3.4 shows a glimpse of this initial mesh.

Parameter	Value
Base grid size	[0.004 , 0.004 , 0.004] m
Embedding scale	3
Embedded layers	3
Initial Number of cells	650823

Table 3.2: Mesh Parameter Summary

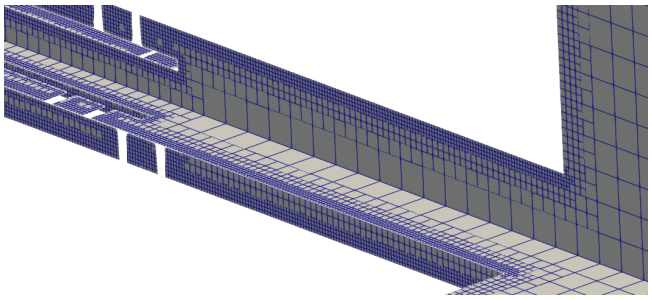

Figure 3.4: Detail of the initial mesh for AMR cases

Once the initial mesh is created, the AMR will act over it to add the necessary refinements based on the sub-grid scale AMR. This feature has been already explained in Section 2.4. A range of sub-grid scales for velocity are used in three different cases, where the coarsest AMR of them represents a small "help" to the base mesh in resolving the complex processes that take place at the entrance of the combustion chamber, and the finest of the meshes tested pushes the case to the pre-established limit of three million cells, which already makes the case run for around fourteen days of physical time using 6 processors. The parameters regarding the AMR mesh controlling are further explained in Table 3.3. Also, in Figure 3.5 it can be seen the difference between the number of cells throughout time for the coarsest and finest approach.

Parameter	Value
Calculation frequency (cycles)	100
Embedding frequency (cycles)	1
Release frequency (cycles)	25
Maximum cells	300000
Regions o apply AMR	Whole domain
AMR Type	SGS
Embed scale	2-3-4
SGS	1

Table 3.3: AMR Parameter Summary

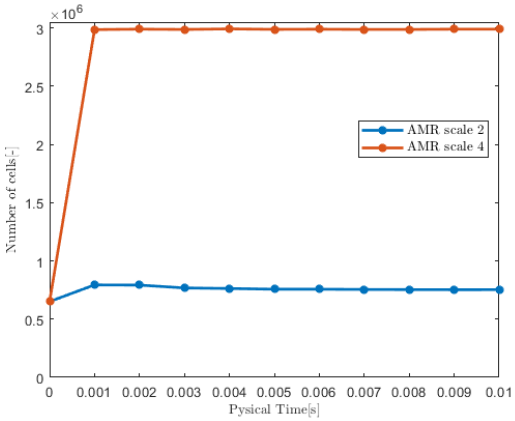

Figure 3.5: Mesh size versus time for finer and coarser AMR meshes

Time: 0.050000 AMR 2

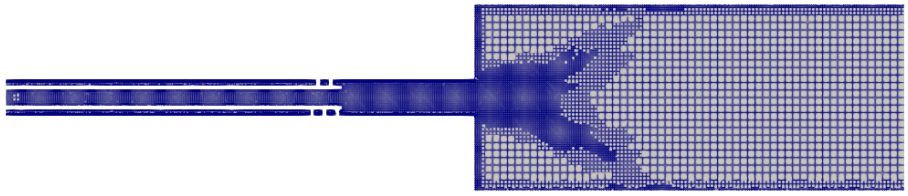

Time: 0.050000 AMR 3

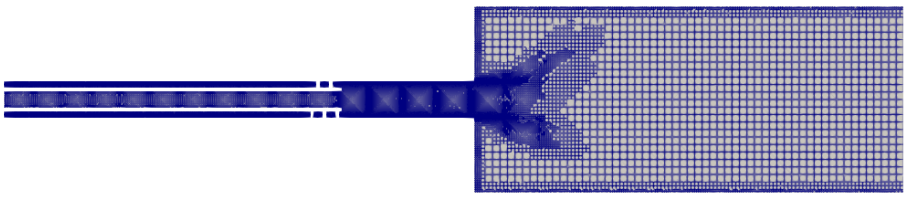

Time: 0.050000 AMR 4

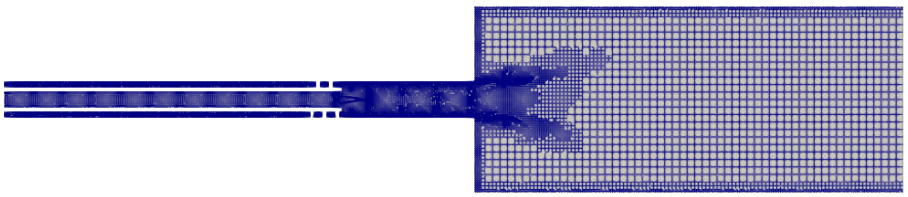

Figure 3.6: Mesh at the final timestep for the three cases

Figure 3.6 shows a comparative view of the three tested meshing approaches. Some of the details that must be noted, apart from the clear view of the different embedding scales used in each case, is the fact that the pre-established number of cells limitation for the whole mesh is forcing the solver not to refine the tail of the swirling structures entering the combustion chamber when using a higher embedding scale. This is, when setting a more ambitious embedding scale that adds more refinement to the entrance of the combustion chamber, the algorithm "runs out of cells" to use in the slower regions of the combustion chamber where also important phenomena can occur. The middle image ($Embedding\_scale = 3$), is also the first result that clearly points to the fact that the case, even when enough time for the stabilization of the flow has passed, manifests some asymmetries which are probably caused by the swirler geometry distribution. This idea will be addressed later in this report in a deeper form.

The results of the three cases back these conclusions. The velocity contours at the same slice of the geometry (Figure 3.7) point that the velocity profile has a different shape when using finer meshes. This is mainly caused by numerical diffusion, the longer refinement of the tail of the vortexes that enter the combustion chamber makes the velocity higher in those zones while this numerical diffusion also damps the asymmetric behavior.

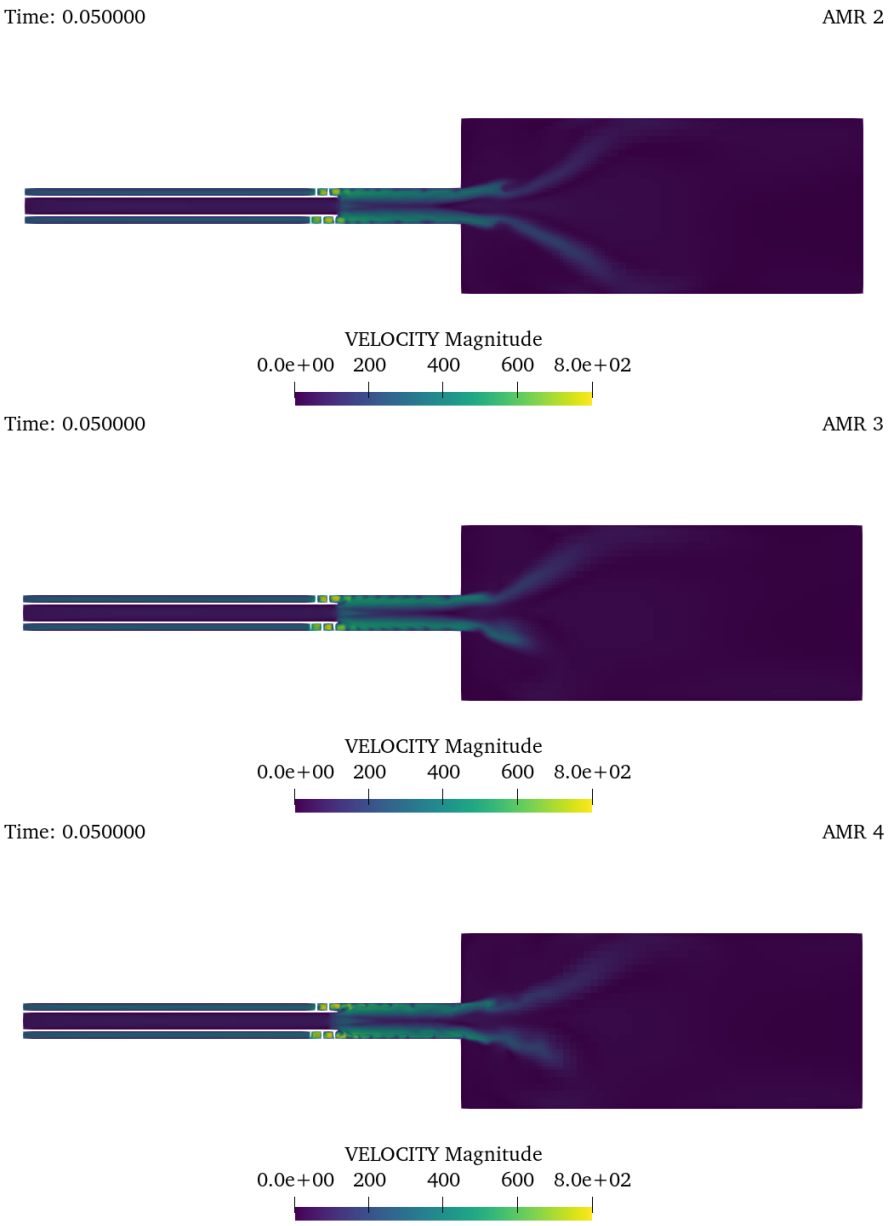

Figure 3.7: Velocity contour at the final timestep for the three cases

As in the non-AMR tests, velocity has been measured at the entrance of the combustion chamber (Point 1 on Figure 3.2) and compared between the different test cases (Figure 3.8). Here the results do not point to an asymptotic mesh convergence as expected, mainly because of the number of cells constraint on the finer refinements of the mesh. The conclusion from the results shown below is that the mesh independence is not reached.

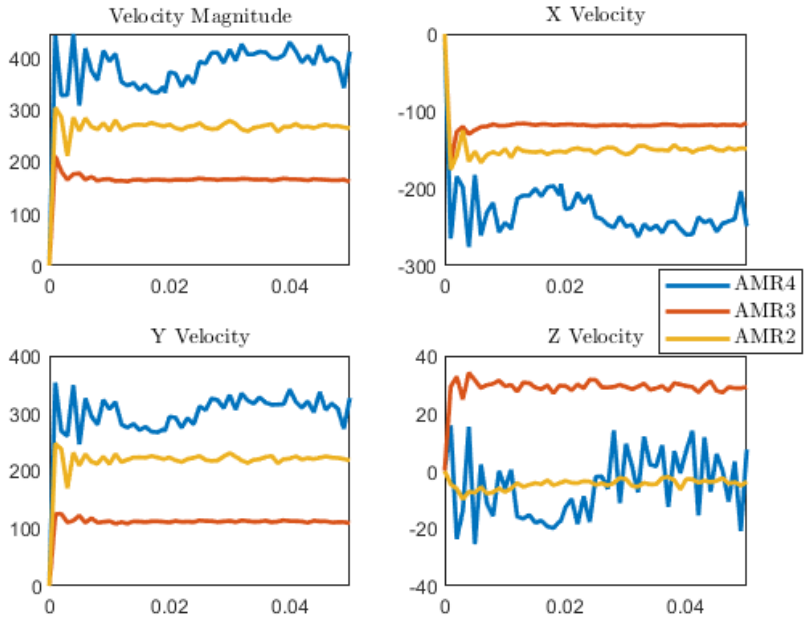

Figure 3.8: Velocity magnitude and component in point 1 for different meshes

The final selection of mesh was done taking into account the presented results. The mesh with ($Embedding\_scale = 3$) was selected, as it represents a compromise solution between the coarser mesh ($Embedding\_scale = 2$), whose numerical diffusion problems can qualitatively change the interpretation of the flow behavior and the finer mesh ($Embedding\_scale = 4$), which was too fine given the number of cells constraint(this was finally decided to be maintained), so the algorithm finds a conflict between properly refine the high-speed areas at the combustion chamber entrance or add some minor refinements to capture the vortex breakdown process, also, the high refinement of this mesh could make some other issues to raise, as the mesh is more refined, the cells are smaller and therefore the timestep has to be lowered to maintain the CFL number on a magnitude the numerical schemes can handle, so with a much smaller timestep there might be some small fluctuations who become artificially increased and end up introducing errors in the simulation, rather than removed.

3.2. LES

When using a LES approach, for the majority of the models, the size of the mesh will affect the filtering of the equations and the modeling of the SGS terms. Hence, it is crucial to assess that the mesh is sufficiently fine to handle this type of simulation with accuracy. Most methods existing to test the quality of an LES mesh need to be done *a posteriori*, but in order to get an estimation of the mesh size, some tools can be used taking advantage of the data from the previously done RANS simulations [12] [34].

Once the results from the RANS simulations are available, the integral length scale can be computed from the κ and ϵ values as in Equation 3.2. As explained in Section 2.5.2, 80 % of the

turbulent kinetic energy must be solved when using the LES equations. Besides, the smallest eddie which can be solved using a mesh with a grid size h, is $l = h/2$.

As can be observed in Figure 2.5, there is a relation between turbulent kinetic energy and eddie size. Therefore, if the aim is to be able to resolve the eddies containing 80 % of the κ, the size of the smallest eddie solved must be around roughly half the size of the integral length scale ($l/l_0 \approx 0.42$). It should be kept in mind that this is not a perfect result, as the reasoning behind it includes some assumptions.

$$l_0 = \frac{\kappa^{1.5}}{\epsilon} \tag{3.2}$$

The application of these ideas to the particular case of this project, suggests a base size of around $6.5 \cdot 10^{-3}$ and a minimum mesh size of 10^{-5}. For the first test which will be done on the LES approach, the base mesh size will be of an order of $4 \cdot 10^{-3}$, and the minimum size will be slightly above the value suggested by these calculations, around $25 \cdot 10^{-5}$. Once this first test case is finished, it will be possible to determine if these previous guesses have been sufficiently accurate or not.

Regarding the *a posteriori* mesh quality assessment, one of the criteria used in this case is the IQ_ν criterion or viscosity index of quality. This criterion calculates the index of quality as stated in Equation 3.3. This criterion considers the numerical discretization error and the subgrid-scale contribution, which are proportional to the grid size. According to the literature ([5], [6]), the lower threshold for this parameter should be around 0.75 for high-Reynolds-number flows in engineering applications.

$$LES_{\mathrm{IQ}_v} = \frac{1}{1 + \alpha_v \left(\frac{\langle v_{t,\ \mathrm{eff}\ f} \rangle}{v} \right)^n} \tag{3.3}$$

On the other hand, the IQ_κ criterion is a direct relation between the resolved and total (modeled + resolved) turbulent kinematic energy (Equation 3.4 [5]). For this criterion, the result should be > 80 % in the whole domain, as previously stated.

$$LES_{\mathrm{IQ}_k} = 1 - \frac{|k^{\mathrm{tot}} - k^{\mathrm{res}}|}{k^{\mathrm{tot}}} \tag{3.4}$$

It is important to highlight the fact that there is no such thing as a mesh independency analysis in an LES simulation, the changes in the mesh will always provoke changes in the results, as they will affect the percentage of total turbulent kinetic energy solved, but it also will change the filters and therefore the subgrid viscosity.

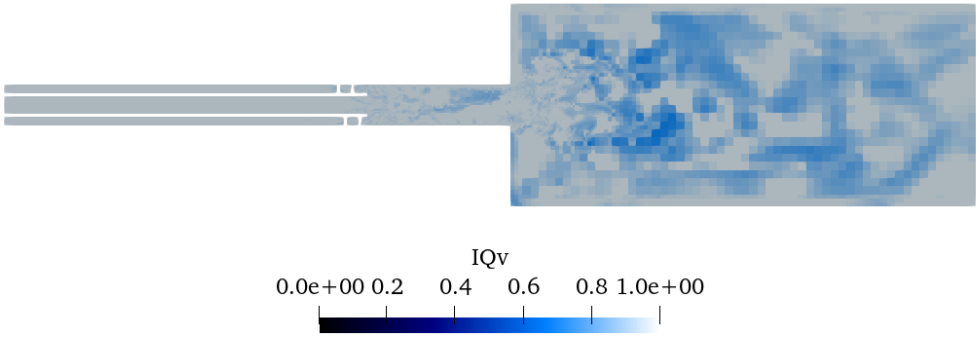

Figure 3.9: Viscosity index of quality contour at the final timestep.

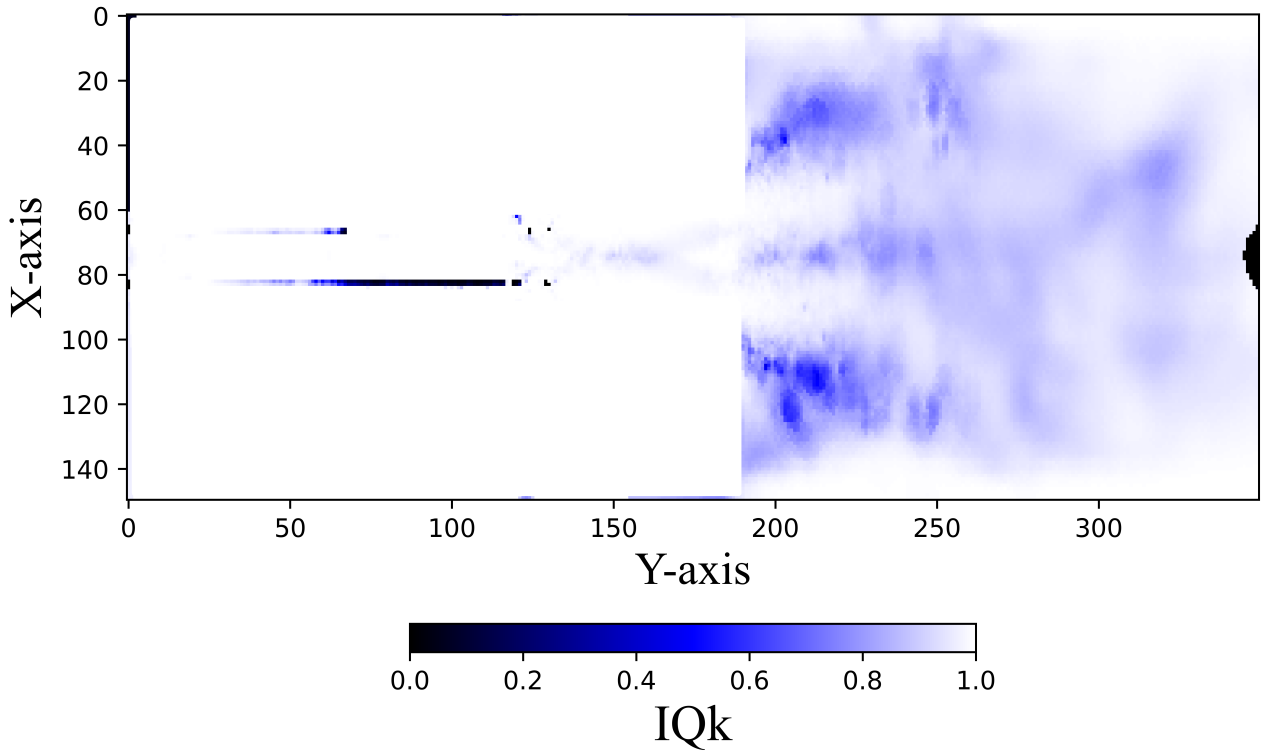

Figure 3.10: Turbulent kinetic energy index of quality contour at the final timestep.

The results of the first mesh tested for the LES approach are displayed in Figures 3.9 and 3.10. For the IQ_ν, some of the values are near the said lower threshold ($IQ_\nu = 0.75$), but the general picture is acceptable. It is important to notice that the lowest quality zones of the domain are not the places where turbulence is higher, but the surroundings of those places, this might seem strange but is caused by the cell cap that was imposed on the AMR algorithm. In other words, the AMR "spends" all the refinement in the highest turbulent zones, following the subgrid criterion given by the user.

Regarding the IQ_κ criterion, the results happen to be a little bit more discouraging. Following the colormap in Figure 3.10, all the places where some blue is appreciated should be refined, in this case, the zones with the worse results are not the same as in the IQ_ν, but the zones where no big vortex breakdown processes happen. This may suggest that those zones, where the lower levels of embedding are applied by the AMR algorithm (or no embedding at all), are not refined enough.

These results point to some changes that should be made in the mesh to meet the usual LES mesh quality assessment tests. However, for the sake of this Thesis, and considering the results on the IQ_κ criterion,the results will be considered good enough to extract some conclusions from them. In further development of this project, the main changes that should be applied to the mesh should be two:

- A review of the base size of the mesh to make the poor values of IQ_κ improve in the low-velocity zones.
- Concerning the improvement of IQ_ν results, the maximum embedding level applied by the AMR should be good enough, but the maximum number of cells should be raised so the AMR can cover a wider region of the domain, capturing the whole vortex breakdown structures.

4. Results

4.1. Mixture analysis - RANS

The variations in gas composition at the inlet provoke a big variation in inflow velocities (this happens because the imposed parameter is mass flow) so it makes sense that this section will directly jump into the results of the different cases run using the RANS approach. The variation between them is solely the H2 mass fractions in the two inflow boundary conditions, so, from these cases, it is expected to obtain a global understanding of how the H2/air proportions injected at both inlets affect the quality of the mixture in the combustion chamber. The DoE was manually modified as the results of the different cases were obtained to explore totally opposite approaches but also to move in the direction where those results showed a chance for a better mixture. A closer look at the parameter definition can be observed in Table 4.1, and also a graphical representation is displayed in Figure 4.1, where the LES case and cases from the previous chapter (3) are represented in the graph together with the RANS mixture analysis to provide an overview about the parameter field where the whole project lays on. Please note that the remaining mass fraction is covered by air(76.7% N_2 *and* 23.3% O_2). It is also worth mentioning that even though the total mass fraction is always the same, the fuel mass fraction is not, so, when analyzing the hydrogen concentration in each case, it should be kept in mind that the upper and more right the cases go in the graph, the more hydrogen is being injected into the domain. This is why the actual values are not as important as trends or ratios.

case ID	Inner Inlet H2 mass fraction [%]	Outter Inlet H2 mass fraction [%]
1	50	50
2	50	0
3	100	0
4	100	50
5	100	25

Table 4.1: H2 mass fraction parameter defintion

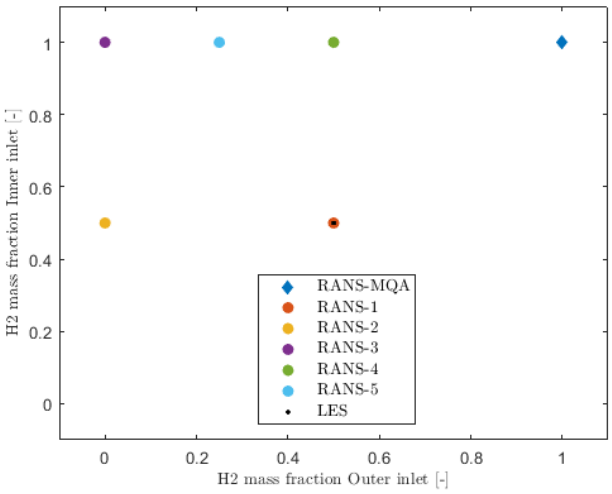

Figure 4.1: Hydrogen mass fraction at inflow boundaries.

Another important thing to acknowledge to ensure accurate modeling, is the presence of discontinuous phenomena in the fluid. As seen in the mesh quality assessment (chapter 3), the velocities in the domain can be quite high, however, this does not necessarily imply the existence of supersonic flow. As it can be seen in Figures 4.2 and 4.3, the flow does not reach the Mach number (Equation 4.1 values where v is the flow velocity and c the speed of sound in the fluid) where these kinds of phenomena occur (shock waves and supersonic behavior should be taken into account when $Ma > 0.9$ [26]). This analysis was made for all cases, but for the sake of brevity, only the results of one of them are presented (The most critical case). The area where high-velocity issues could be a problem is the area around the flow swirlers, but Figure 4.3 provides an image respectively before, in the middle, and after this geometry where it can be confirmed that the Mach number is well below the said threshold.

$$Ma = \frac{v}{c} \tag{4.1}$$

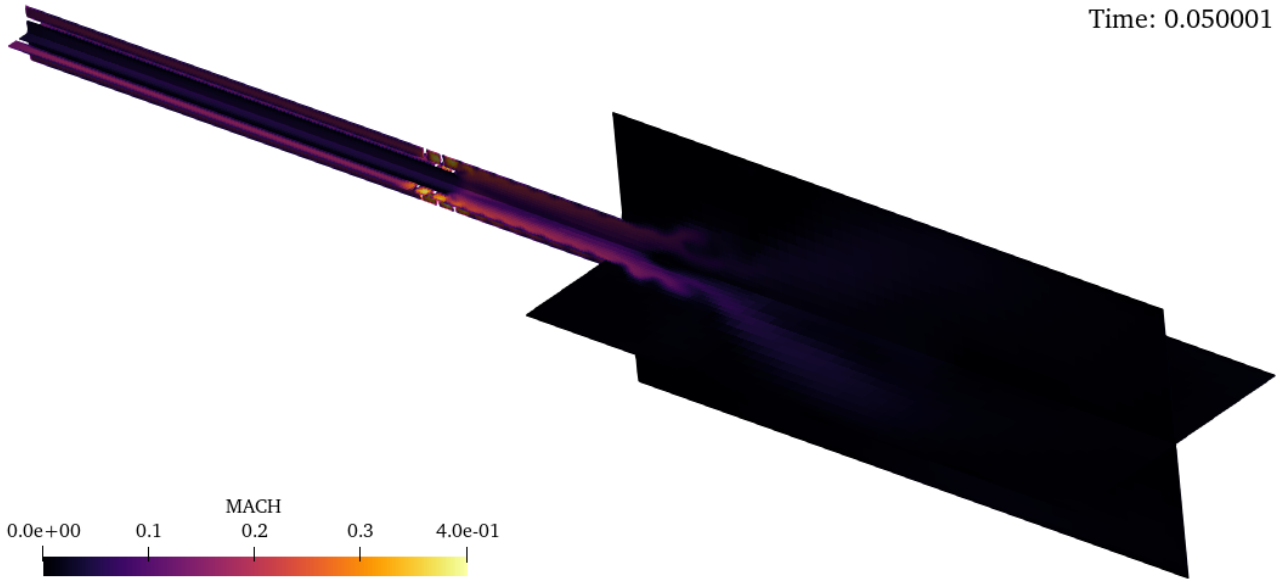

Figure 4.2: Mach number contour at mid-X and mid-Z planes slices.

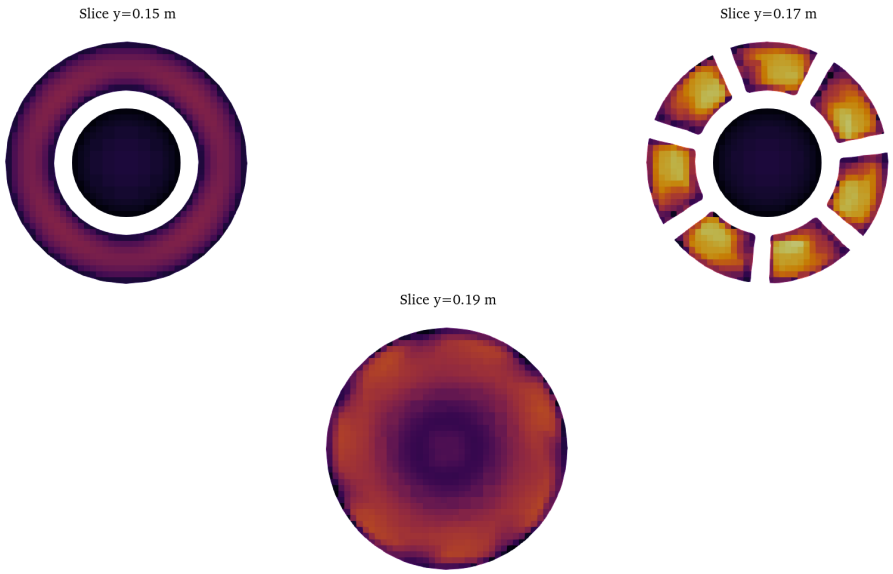

Figure 4.3: Mach number contour at different Y-plane slices.

For the analysis of the results, apart from general contours and other post-processing techniques, a set of pre-defined planes and points are defined inside the combustion chamber, the values of velocities and mass fractions in these places will be the ones that allow the comparison between the different cases previously described. The geometrical parameters of the points and lines can be consulted in Tables 4.2 and 4.3 respectively, and a graphical representation of bot is displayed in Figure 4.4. Apart from the described planes, the centerline axis of the geometry along the whole domain is also used to evaluate the results.

Point #	**X position [m]**	**Y position [m]**	**Z position [m]**
1	0.05	0.25	0.728
2	0.05	0.27	0.728
3	0.05	0.27	0.748
4	0.05	0.29	0.728
5	0.05	0.29	0.748

Table 4.2: Probe point location

Line #	**Y coordinate position [m]**
1	0.255
2	0.26
3	0.27
4	0.28
5	0.29

Table 4.3: Line Y position (Along the X and Z directions, the lines cover the whole domain)

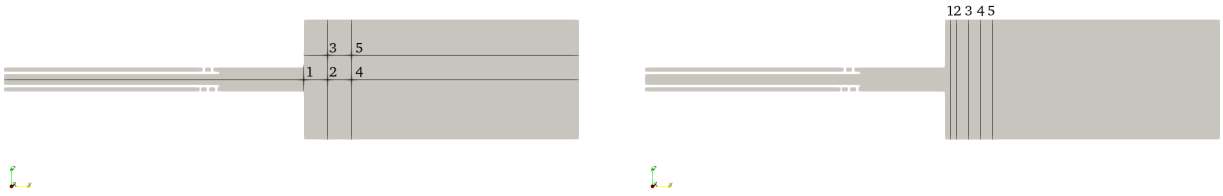

Figure 4.4: Points (left) and lines (right) location in an x-plane slice of the geometry

It is important to clarify that, if not stated otherwise, the data collected will correspond to the last timestep of the simulation (*t=0.05 s*). at this moment the flow should have reached a quasi-stationary behavior for most of the variables, as it will be exposed in the existent graphs inside this section. All the data plotted in this section has been analyzed to ensure that there is no notable difference between the plotted timestep and the previous one.

4.1.1 Case 1

This case is run on a 50 % hydrogen mass fraction on each inflow, the pre-established mass flow rates imposed at the inflows make the velocity on the outer pipe much larger than in the inner pipe. This will lead to a high-swirling flow (remember that the swirlers are only affecting the flow on the outer pipe), which will also lead to a relatively good mixing of the combustion chamber, but also will make it more difficult for the case to stabilize.

The first thing that draws attention from the results, is that for a given time, the contours on the domain are not symmetric with respect to the centerline(for example velocity contours at Figure 4.5). This is because the perturbations in the flow field caused by the swirler geometries are not constant, but cyclic, and this can also be noted when looking at the temporal evolution of the velocity in the points in Figure 4.6. This result may suggest using a different swirler configuration (varying the number of swirlers and changing their angles) could eliminate this impact. However, this cyclic behavior has a different effect on the hydrogen concentration (Figure 4.7). While at point 1, the impact on the unsteadiness is negligible, at point 5 it can be seen a more fluctuating behavior, even though there seems to be a trend towards stabilization in the species mass fraction. The reason for these differences comes from the locations of the points in the domain (Figure 4.4), point 1 is right at the entrance of the combustion chamber, so once the initial air mixture is washed out of the domain, point 1 will basically just have the mass fraction of the upstream inflows, whereas point 5 is located at the place where the vortex breakdown process takes place, and therefore will suffer from as many instabilities as the upcoming flow shows. It is important for the combustion process that there are no "bubbles" of high fuel mass fraction because this could lead to abnormal combustion. Please note that only points 1 and 5 are shown here because the behavior of the rest of the points was placed between these extreme cases.

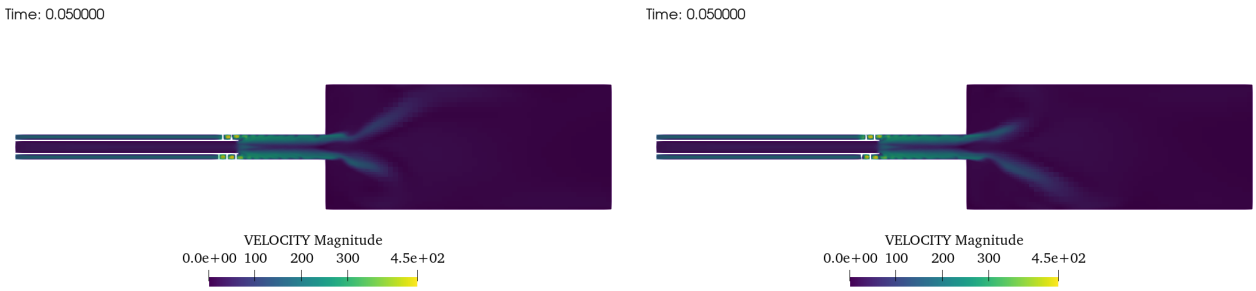

Figure 4.5: Velocity contours on X-plane (left) and Z-plane (right) slices of the geometry

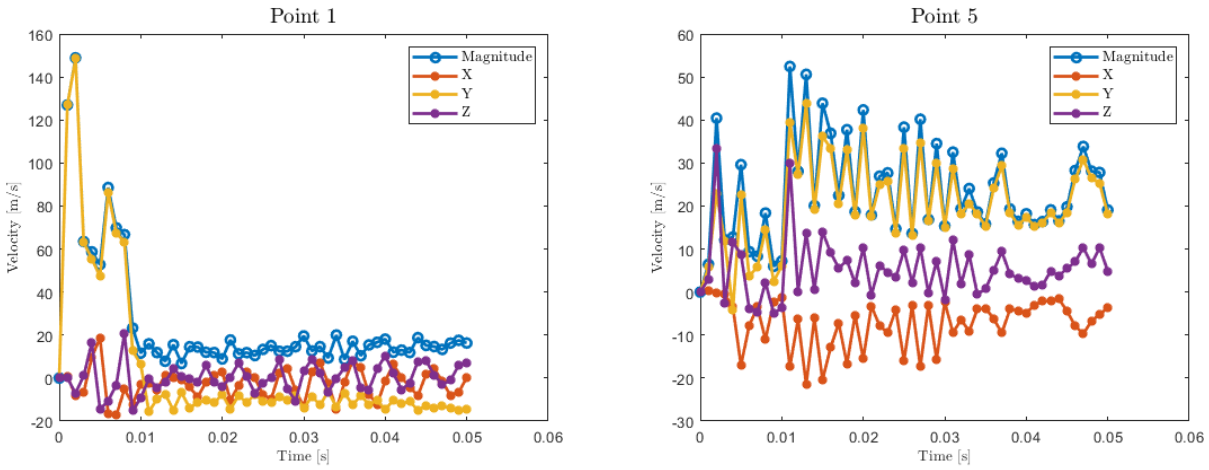

Figure 4.6: Velocity at point 1 and point 5 over time

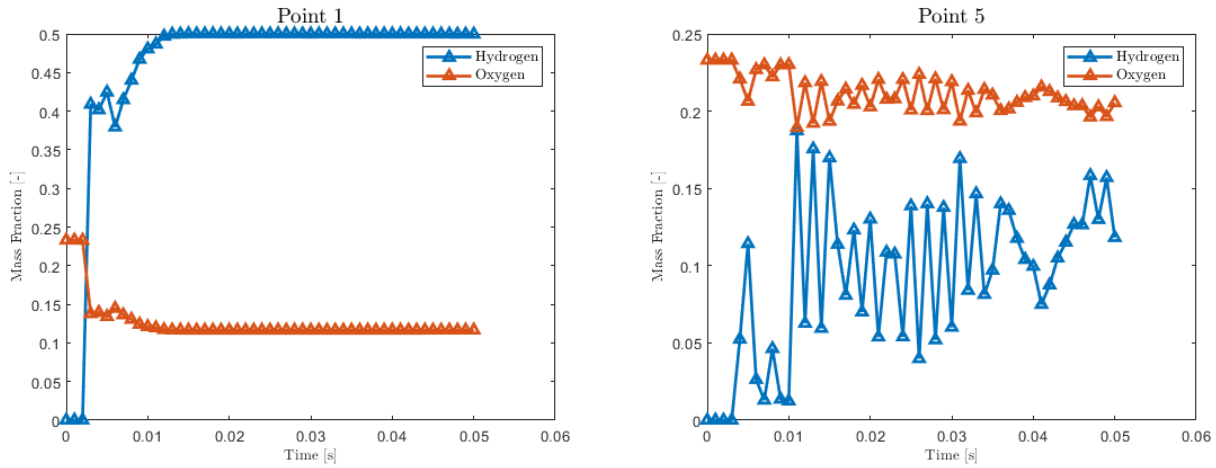

Figure 4.7: Mass fraction at point 1 and point 5 over time

The velocity profile along the domain centerline (Figure 4.8), can show some light into the analysis of the flow's development inside the domain. The centerline axis belongs to the inner pipe, which is why the velocity profile stays relatively constant until 0.17 m. Then, the bigger velocity of the outer pipe drags the flow, augmenting the velocity drastically at first, then stabilizing near 60 m/s. At the distance of 0.25m, the combustion chamber starts, and the vortex breakdown structures created in the combustion chamber make a recirculating bubble appear and the axial velocity drops to negative values, these vortex breakdown processes are often common to high-Swirl number (Equation 4.2)[4] flows. The Swirl number accounts for the difference between the momentum in the tangential direction and in the axial direction. The theory for explaining vortex breakdown is quite complex and has lots of approaches (wave phenomena, flow stagnation, stability theory...)[21], but this is outside the scope of this project.

$$S = \frac{\int_0^\infty \rho u u_\theta 2\pi r^2 dr}{R \int_0^R \rho u^2 2\pi r dr} \tag{4.2}$$

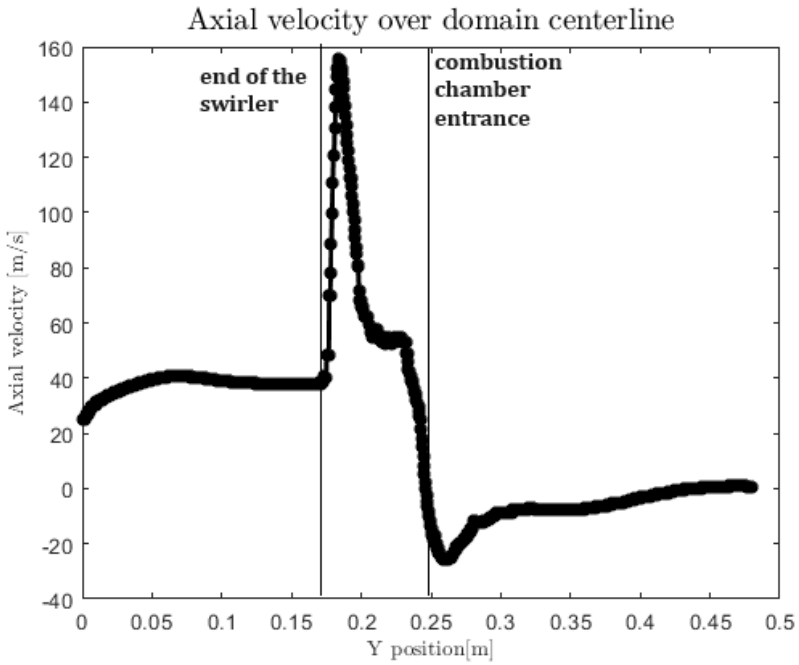

Figure 4.8: Axial velocity over domain centerline (Y axis)

In Figure 4.9, an idealization of the two main vortex breakdown structures is displayed.

- Inner Recirculation Zone (IRZ): Located right along the axis of the swirler, this recirculation bubble appears for large values of Swirl number (typically above 0.6) ([3]) and results from the natural radial pressure gradient generated by the guided rotating flow (large tangential velocity component of the flow) as well as the flow expansion at the entrance of combustion chamber. Indeed, at the expansion, the radial pressure gradient and axial velocity components suddenly decay producing a negative axial pressure gradient, which is the reason for this structure to form.

- Outer Recirculation Zone or Corner Recirculation Zone (CRZ): In confined configurations, the same sudden expansion of the flow at the chamber inlet is stopped by recirculating bubbles which are formed near the corners of the rectangular geometry, in this case. This second structure is not that noticeable because of the lower magnitude of velocity in these zones. If a longer runtime was chosen for this simulation, probably the further stabilization of the flow would make this phenomenon more obvious when looking at the contours.

These phenomena are illustrated in Figures 4.10 and 4.11 for the specific case of the burner analyzed in this project. The last time-step recorded, which is the one in the images, shows both an IRZ (around the centerline of both slices) and a CRZ (lower part of X plane and upper part of Z plane). More specifically, at Figure 4.10, the yellow area represents the zones where the axial velocity is negative.This recirculation zone enhances the mixing and combustion and acts as an aerodynamic flame holder [4] [2].

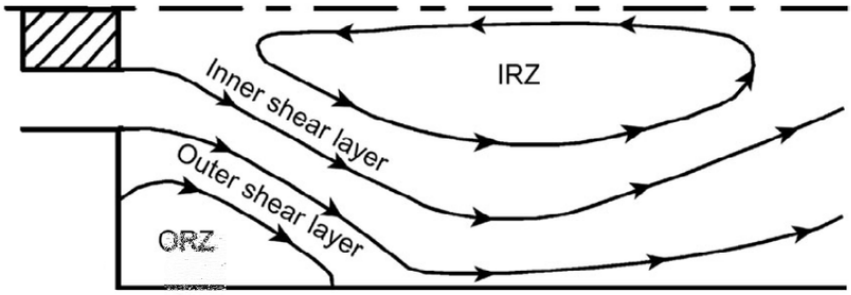

Figure 4.9: Swirling flow structures (Extracted from [33])

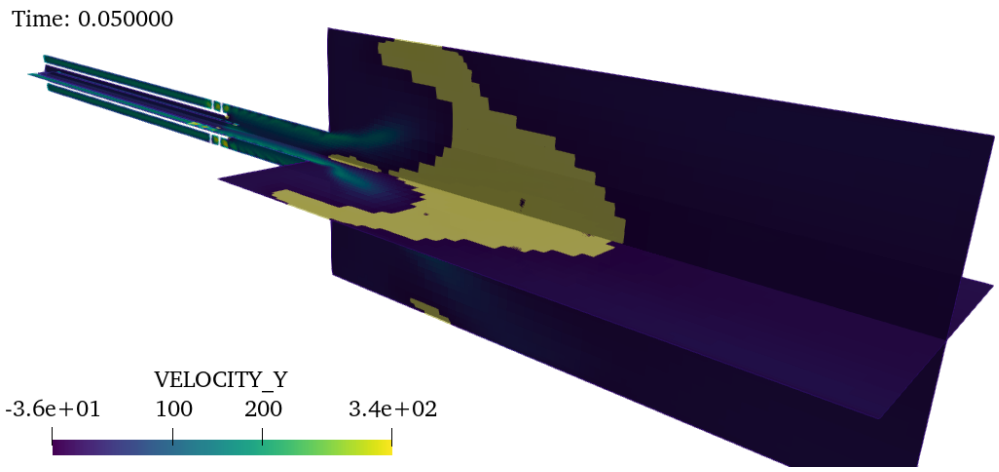

Figure 4.10: Recirculation zones (in yellow) over velocity contour

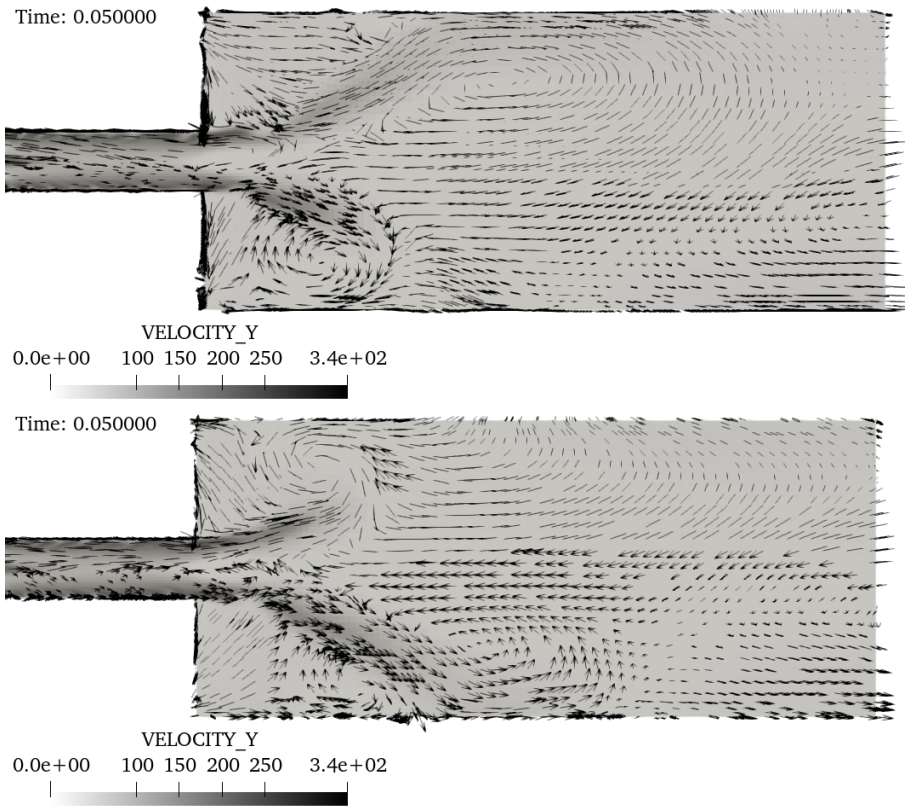

Figure 4.11: Plane X (top) and Z (bottom) slices with velocity vectors

Continuing with the turbulent structure analysis, by looking at the combustion chamber sliced at different Y positions (Figure 4.12), the formation of these vortex breakdown structures can be appreciated, where the initial circle-shaped velocity profile expands in the combustion chamber as the axial velocity at the core starts getting more and more negative, which is represented with darker orange tones, and the CRZ also emphasizes as the distance grows from the combustion chamber inlet compared to the inlet pipe diameter (D).

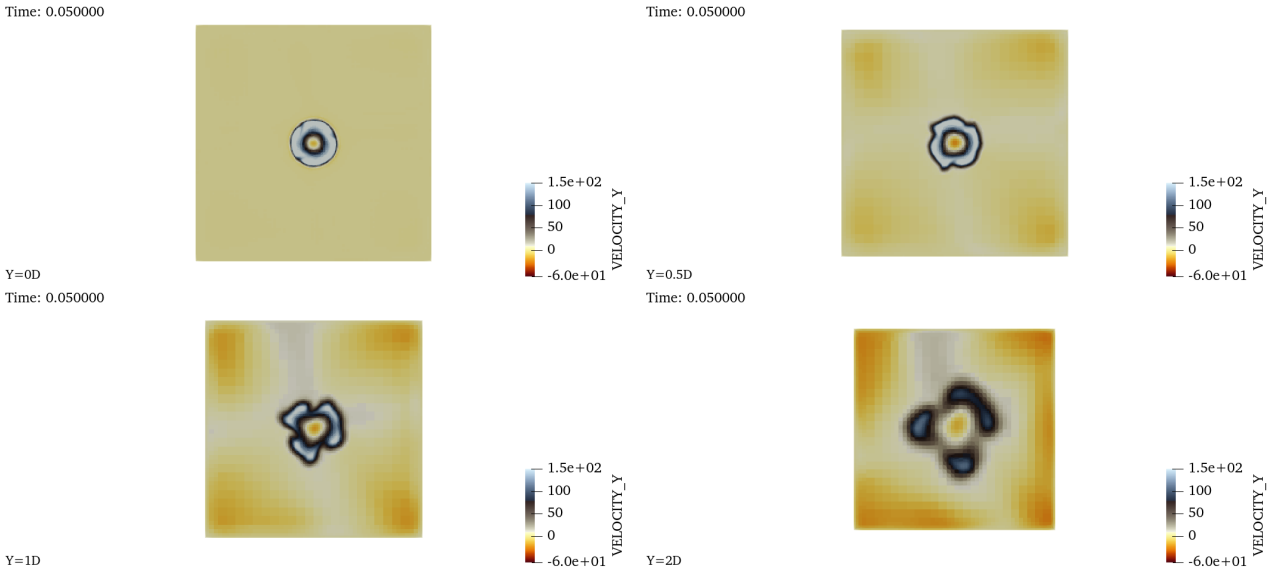

Figure 4.12: Axial velocity profiles for Y-plane slices along the combustion chamber

Along with the centerline axial velocity analysis, the perpendicular lines also show interesting features of this case. In Figure 4.13 it can be observed that the velocity profiles evolve

into a “M” shape, whose flanks steadily broaden as the flow advances through the combustion chamber. The velocity profile transports the hydrogen mass fraction and is the cause for this scalar having also a “M” shape distribution far away from the entrance. This effect enhances mixing quality as makes the fuel spread in the combustion chamber, compared to the profile seen in lines 1 and 2, where there is a sharp difference between the ”jet” entering the chamber and the outside of it.

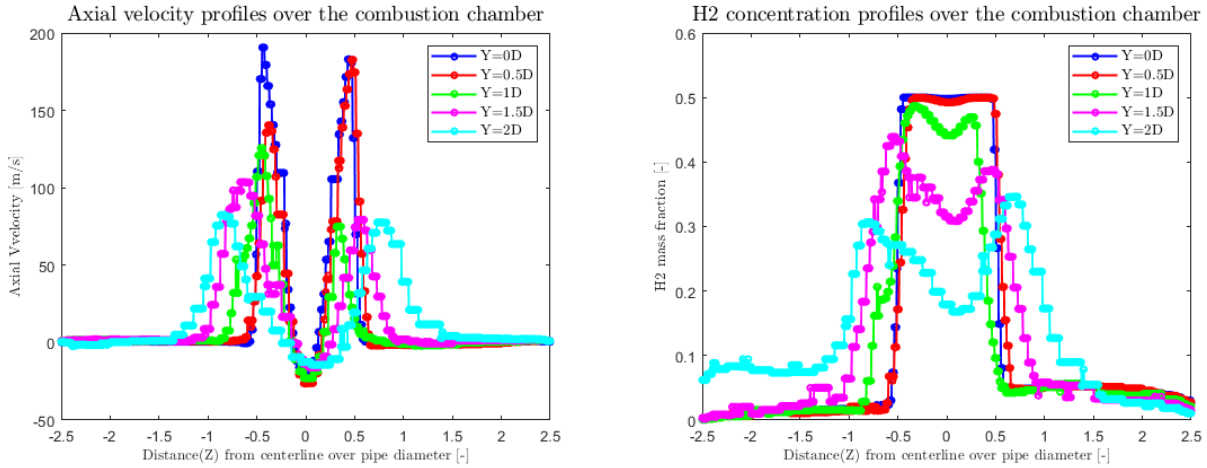

Figure 4.13: Velocity and mass fraction profiles over the dimensionless distance at probing lines

Following the topic of species mass fraction distribution, not only the hydrogen (fuel) is important but also the oxygen (oxidizer), as both are required for the reaction, and the ratio between both can be more important than one mass fraction distribution alone. This kind of cold-flow super-rich cases are often experimentally tested with argon instead of air, or helium instead of hydrogen, as those are inert gases and ensure the combustion is not happening for safety reasons. The lack of experimental parameters to state the most suitable combustion regime for this specific case, makes the smooth distribution of both fuel and oxidizer the most interesting analysis on this species distribution topic, as the excess or absence of one of those can prevent the species in that specific zone from being burnt, which will negatively affect the performance and efficiency of the engine.

4.1.2 Case 2

As seen in Figure 4.1, this second case has the same concentration of hydrogen at the inner inlet (50%) but has no presence of it on the outer inlet. This, as previously explained in Section 2.7.1, has an impact also on the velocities in the outer and inner pipes, which ultimately will influence which of these streams will drive the flow behavior when they come together.

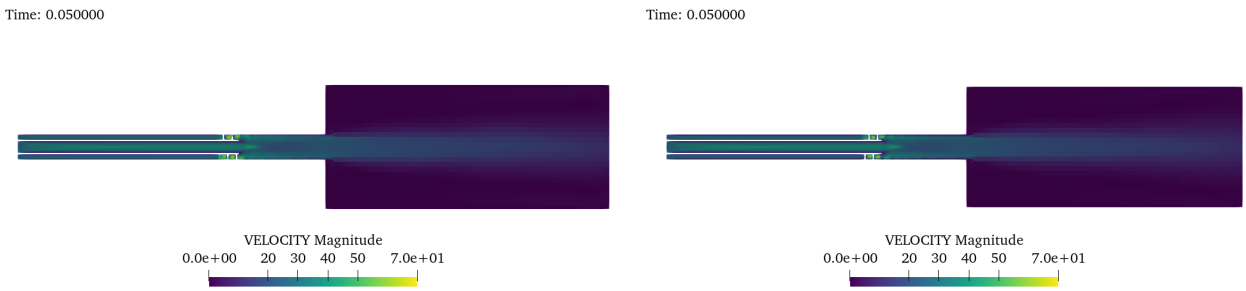

Figure 4.14: Velocity contours on X-plane (left) and Z-plane (right) slices of the geometry

Following the same roadmap as in the previous case, a quick look at the velocity contours reveals that they are totally different from the previous case. When comparing Figures 4.5 and 4.14, these differences arise. The whole velocity magnitude is approximately one order of magnitude smaller, moreover, in this case, the velocity on the outer inlet is not big enough to drag the gas in the inner inlet, resulting in the swirling flow being secondary rather than the main feature on the case. This case is more a pure jet stream than a swirling flow and hence some of the setup decisions that were made are not the correct modeling approaches for this case. For example, the AMR based on velocity as defined in Section 3, has no effect here because the velocities are not big enough to trigger the scaling, consequently numerical diffusion plays a huge role in the jet behavior inside the chamber. Another proof of this is the velocity evolution at the probing points, where points inside the central axis have a constant, uniform velocity magnitude where the axial component is always positive (Points 2 and 4 in Figure 4.15) whereas points separated one pipe diameter (0.02 m) from the central axis (Points 3 and 5 in Figure 4.15) show some oscillations around negligible velocity magnitudes, and also small values of non-axial velocity (components X and Z). This jet-type behavior, apart from being detrimental to mixing performance, could also make problems such as flame blow-off arise. This of course affects mass fractions, leaving all the mixture work for diffusion, which as can be seen in Figure 4.16, reaches a fast steady state at the centerline points, however, the hydrogen does not even get to Point 3 location, which means that the volume of the combustion chamber where combustion can happen is really low in percentage.

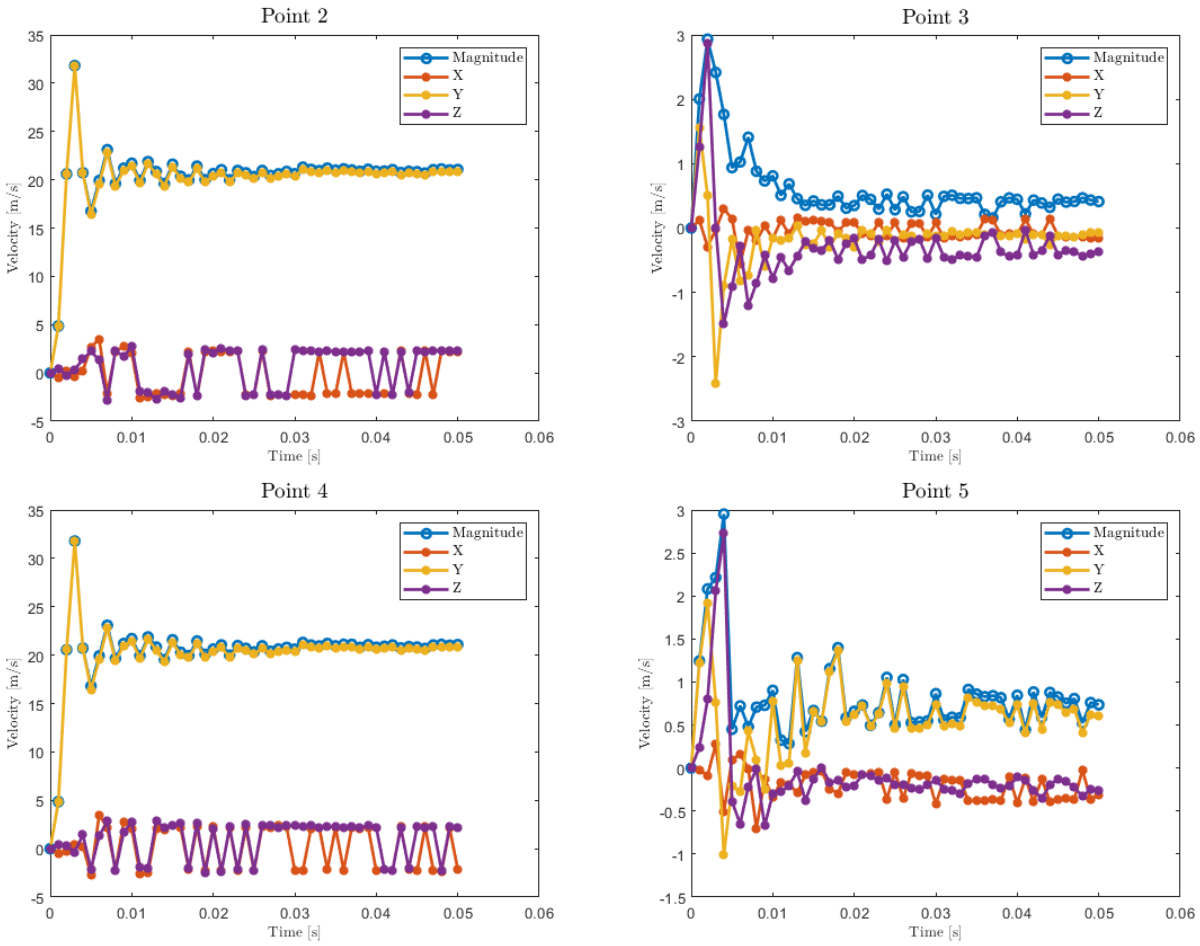

Figure 4.15: Velocity at points 2, 3, 4, and 5 over time

The data exposed in Figure 4.17 reinforces the idea of the inner outlet flow being decelerated by the outer inlet flow and not dragged in this case, compared with Figure 4.8, the velocity

after both streams mix is slower than the velocity before now. Also, as no vortex breakdown structures are formed, diffusion makes the velocity decrease steadily inside the combustion chamber. Also the sharp gradients both in velocity and mass fraction when plotting them on the probing lines (Figure 4.18), which are rectangular, rather than "M" shaped, prove that the mixing quality is not good using this input parameters. Note that this study has chosen to fix the mass flow rate at both inlets and focus on the mass fraction percentages for parameter analysis, but these values could be changed on both inlets if aiming to achieve a better performance of the system while still using these mass fraction percentages.

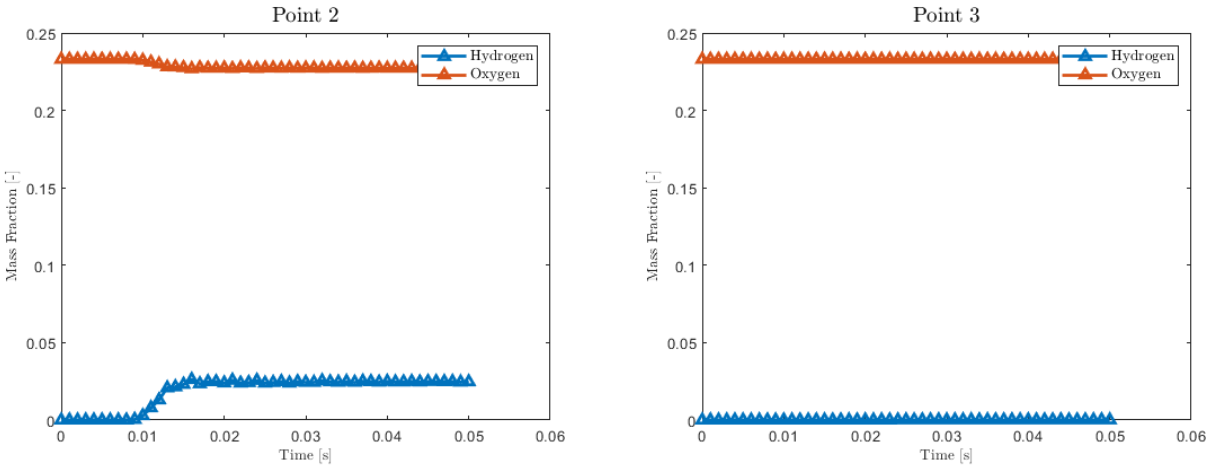

Figure 4.16: Mass fraction at point 2 and point 3 over time

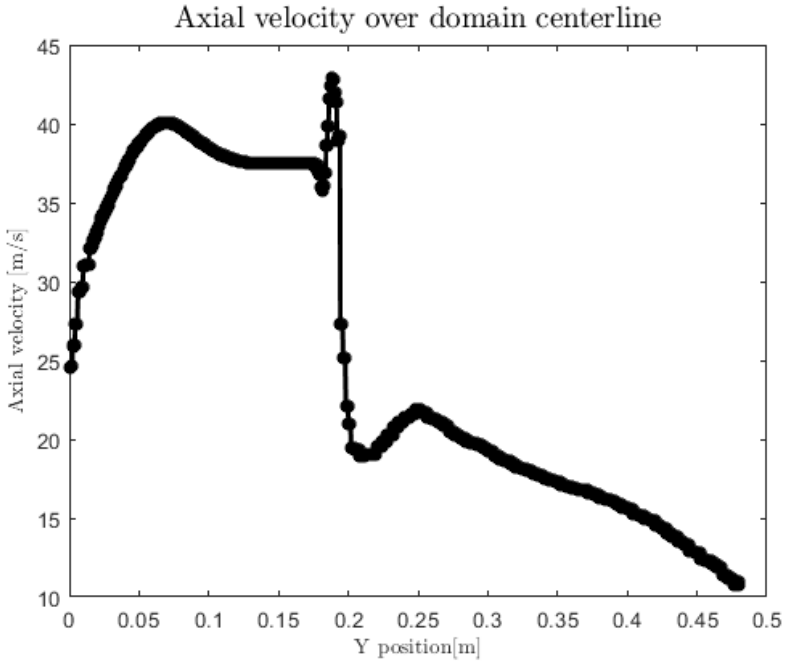

Figure 4.17: Axial velocity over domain centerline (Y axis)

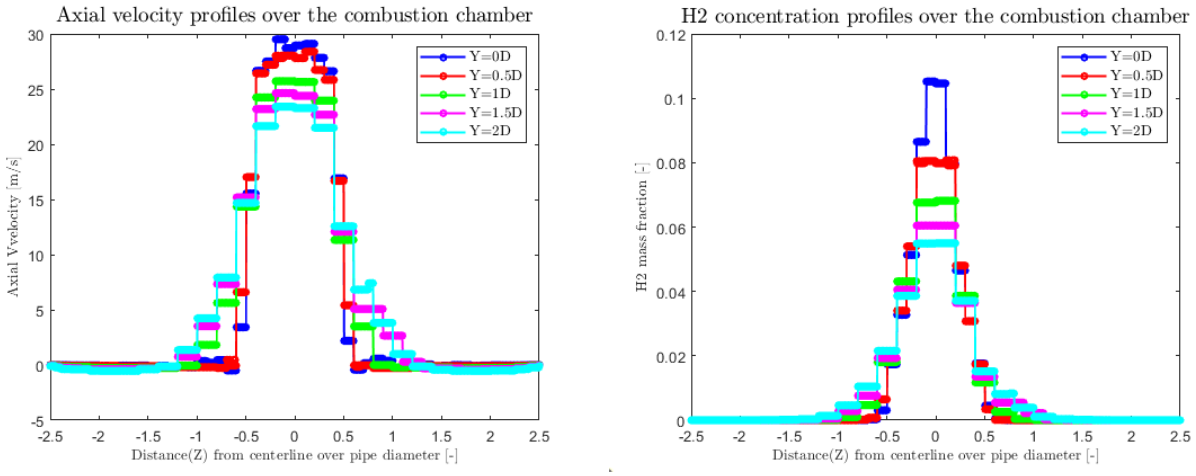

Figure 4.18: Velocity and mass fraction profiles over the dimensionless distance at probing lines

4.1.3 Case 3

The third analyzed case maintains the full air injection on the outer inlet but rises up the inner inlet hydrogen mass fraction from 50 % to 100 % compared with the second case. This case exhibits again poor behavior on the swirling performance, as the velocity in the inner pipe is much bigger. Therefore the effects of the swirlers are negligible in the flow entering the chamber.

This can be stated by looking at the results and comparing them to the ones obtained from Case 2, despite the fact that in this case, as the quantity of hydrogen injected is higher, the mixture is richer in the neighboring of the centerline (Point 2 in Figure 4.20), whereas outside this zone the hydrogen has a minimal presence (Point 3 in Figure 4.20). Regarding the velocity profiles over time in those points (Figure 4.19), they are also alike to the ones seen in the previous case, but in this case, the non-axial velocities seem to have a less fluctuating nature at the centerline (Point 2 in Figure 4.19), probably resulting from the higher velocity in the jet which also experiences this kind of behavior but in a further position inside the chamber.

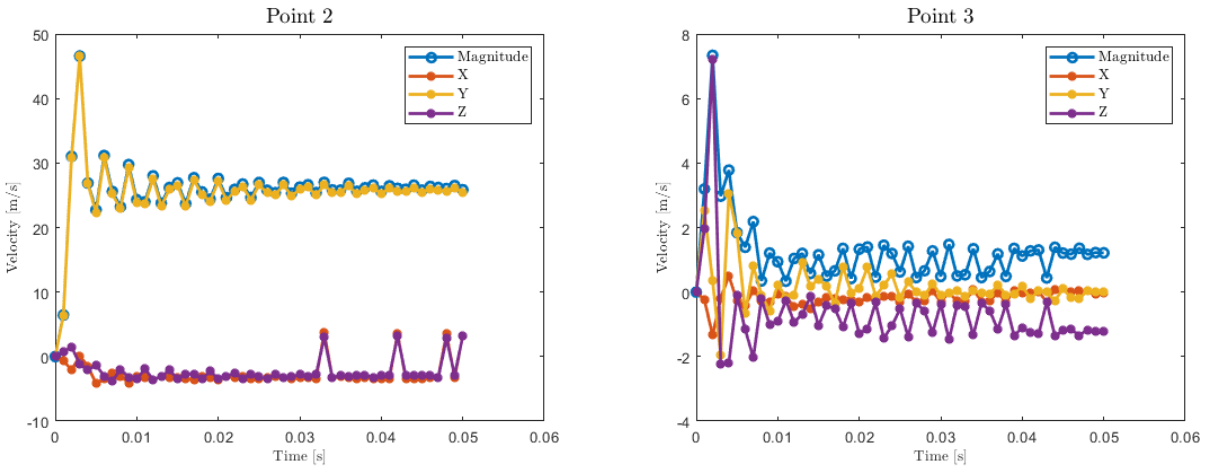

Figure 4.19: Velocity at points 2 and 3 over time

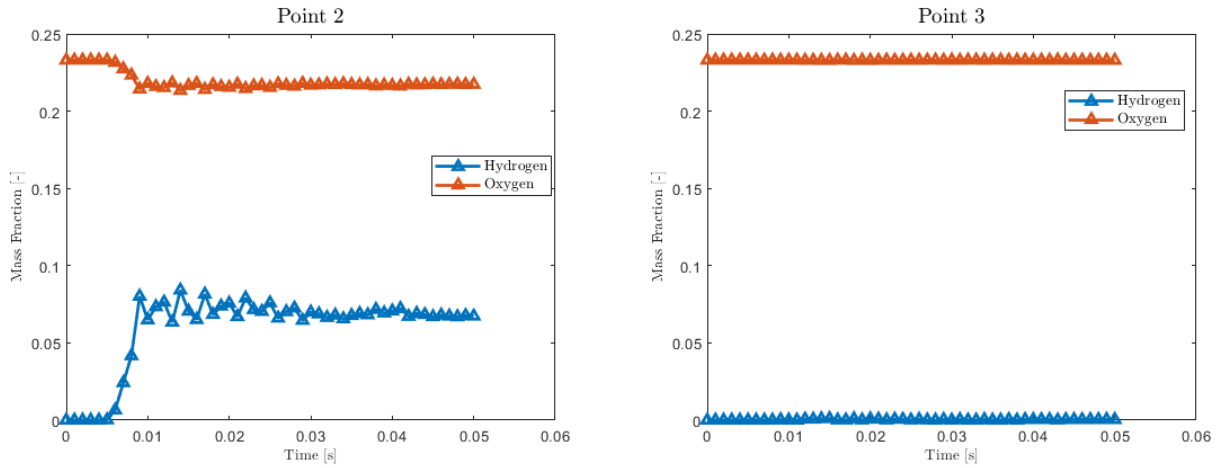

Figure 4.20: Mass fraction at point 2 and point 3 over time

4.1.4 Case 4

This fourth case is indeed a correction from the results obtained in cases 2 and 3, aiming to determine the zone in the mass concentration map (Figure 4.1) where the swirling system behaves according to expected. In this case, from the outer inlet the mass fraction of hydrogen is 50 % while in the inner one, it is full hydrogen.

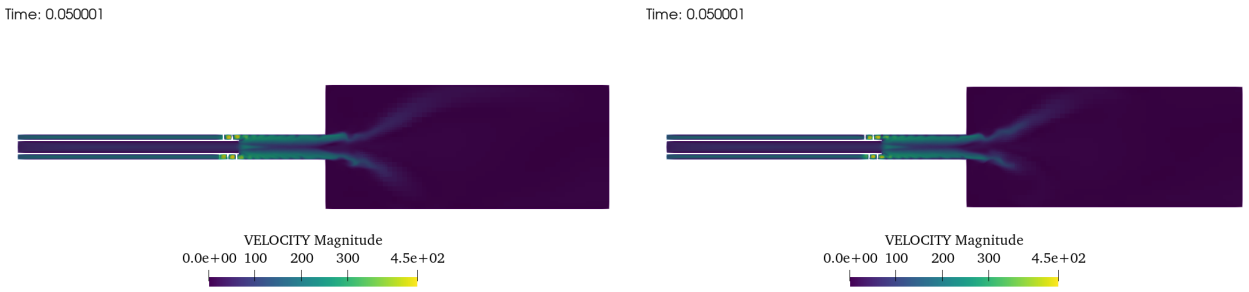

Figure 4.21: Velocity contours on X-plane (left) and Z-plane (right) slices of the geometry

In Figure 4.21, it can be appreciated that, unlike cases 2 and 3, in this case, the outer pipe carries enough momentum to impose a swirling motion that ultimately affects the flow at the entrance of the combustion chamber, being actually closer to case 1.

If the velocity at the probing points is analyzed (Figure 4.22), it can be seen that at the entrance of the combustion chamber (Point 1), the velocity profile converges to a cyclic profile (especially for the X and Z components). This cyclic behavior means that the asymmetries created by the swirlers vary over a certain period of time. If these variations are strong enough to be present also in the hot flow case when combustion happens, the distribution of the swirlers could be tuned in order to achieve a certain pattern that could minimize the thermal fatigue for the components inside the combustion chamber. While advancing inside the combustion chamber through the centerline (Points 2 and 4), these cyclic patterns are influenced by recirculations, numerical errors, and interactions with other streams, but they still can be guessed in the non-axial velocity components. Lastly, outside the centerline, the trend also affects velocity components (Point 5), except for Point 3, where these fluctuations seem to have no impact because it is too far in the radial coordinate to suffer from these effects.

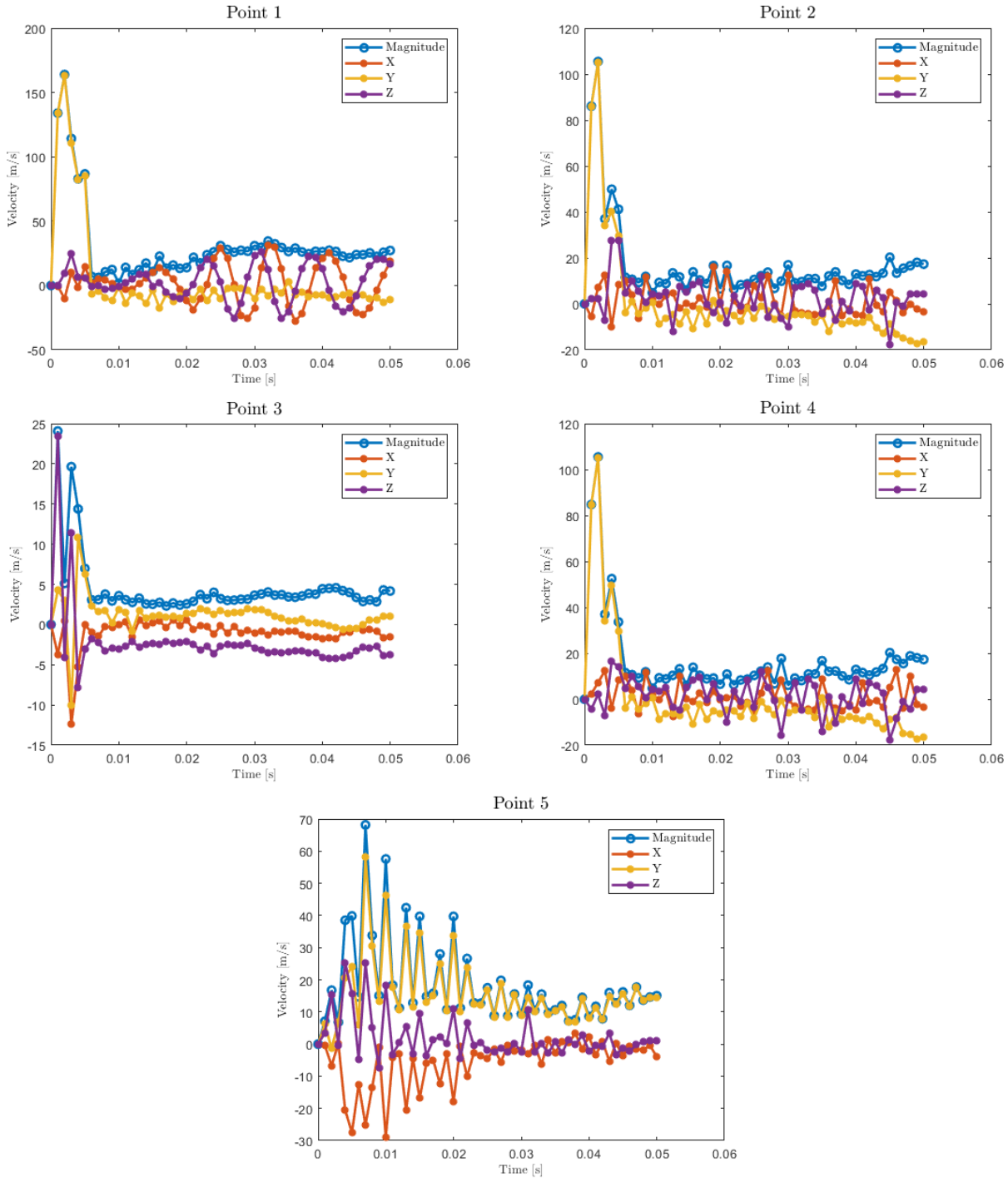

Figure 4.22: Velocity at points 1, 2, 3, 4, and 5 over time

It has to be borne in mind that these cycles are in X and Z velocity components, so the fluctuations whose average is zero only mean that the "center" of the vortex breakdown structures is not always the centerline of the chamber, but evolves over time. As the X and Z components of velocity, for a constant tangential speed, are positive in half of the domain and negative in the other half, these fluctuations that are seen in the graphs are only slight variations on the swirling center, which is eccentric over time, so the probing points move from the part where he velocity component is positive to where it is negative (Note that the peaks have the same absolute value). These fluctuations also seem to be slightly losing frequency and amplitude while gaining length, this might suggest that the flow might get to a more stable solution if the case is run for a long time. In Figure 4.23 this idea is illustrated, where the black areas are where the X component of velocity is near zero, and the lines indicate the geometrical center

of the combustion chamber. It can be seen that for two different timesteps, separated by half wavelength in time, this black line that separates positive from negative velocity zones, has moved from one side of the center to the other, indicating that now in the center point the X component's velocity sign has changed. This explanation applies also to cases 1 and 5, of course with different magnitudes because of the velocity differences.

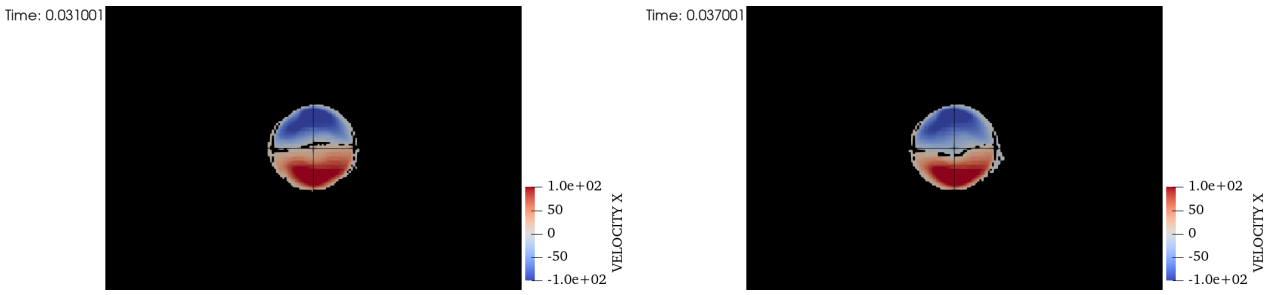

Figure 4.23: X-velocity contour with a near-zero threshold at the combustion chamber inlet

However, this cyclic behavior is not clearly reflected in the species concentration, as can be seen in Figure 4.24. If these results are compared with Figure 4.7 from case 1, the shape of the mass fraction profiles is very much alike between both cases. Therefore it can be concluded that the effects of the relatively important changes in the velocity profiles do not transform into big changes in the fuel-oxidizer distribution.

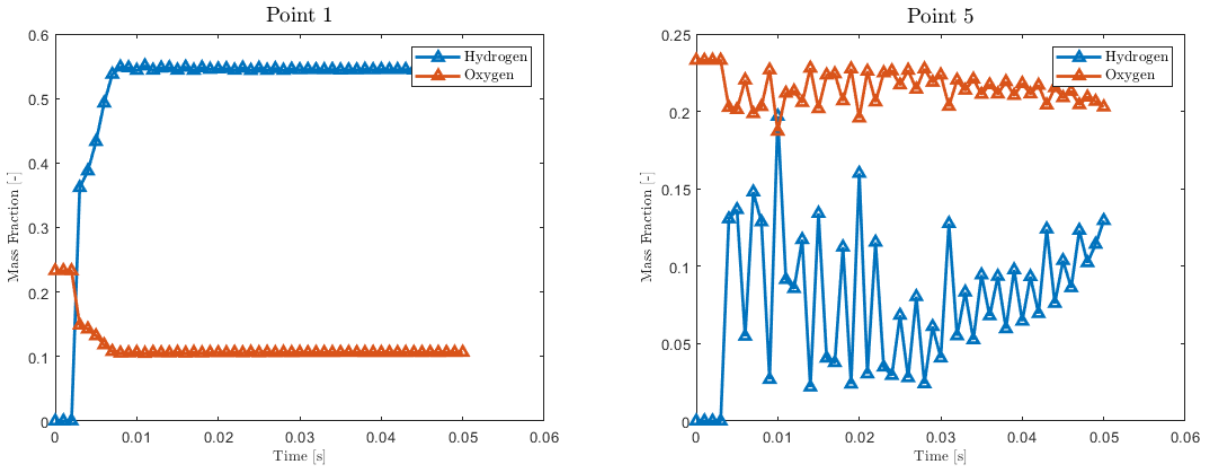

Figure 4.24: Mass fraction at point 1 and point 5 over time

Going back to the velocity profiles, when analyzing the axial velocity over the domain centerline (Figure 4.25) and comparing it, again, with case 1, (Figure 4.8), the qualitative output is very similar except for the zone just after both outer and inner pipes come together (around Y=0.21 m). In this case, the higher velocity in the outer inlet forces the inner stream to accelerate faster, making the flow less stabilized by the time it enters the combustion chamber.

In Figure 4.26, the results at probing lines both for axial velocity and hydrogen mass fraction are shown. In this case, it can be observed a great asymmetry in velocity profiles that has an effect also in the species distribution. This is especially important because this asymmetry is not stable inside the combustion chamber. In the lines that are closer to the inlet (Lines 1 and 2), the positive side of the X axis has larger values of velocity axes, whereas it is the opposite for lines placed right after (Lines 3 and 4). Furthermore, the last probing line (Line 5) shows a more symmetric distribution, so it can be said that this asymmetry is lost in the vortex breakdown process (it could be impacted by the low stabilization of the flow entering

the combustion chamber explained above, as this stabilization inside the combustion chamber is stronger in case 1 (Figure 4.13)). However, the "M" shaped profile of velocity is maintained in all of them, confirming the existence of an IRZ structure.

The mass fraction distribution profile supports this idea of case 4 being more unstable as it is a much more changing profile, showing a large number of asymmetries and fluctuations on the "M" shape profile. These asymmetries are present all the way through the simulation, however, their specific shape may change from one timestep to another. As seen in case 1, the system struggles to make the species distribute correctly early in the combustion chamber (Line 1 in Figure 4.26). This could be an issue in the real-world functioning of these devices as it is normally in these places where combustion occurs. In order to maximize the performance here, the range of radial coordinate dimension where hydrogen has an important concentration should be as wide as possible. The result of this parameter is highly dependent on the shape and intensity of the CRZ, making it a phenomenon as important as IRZ.

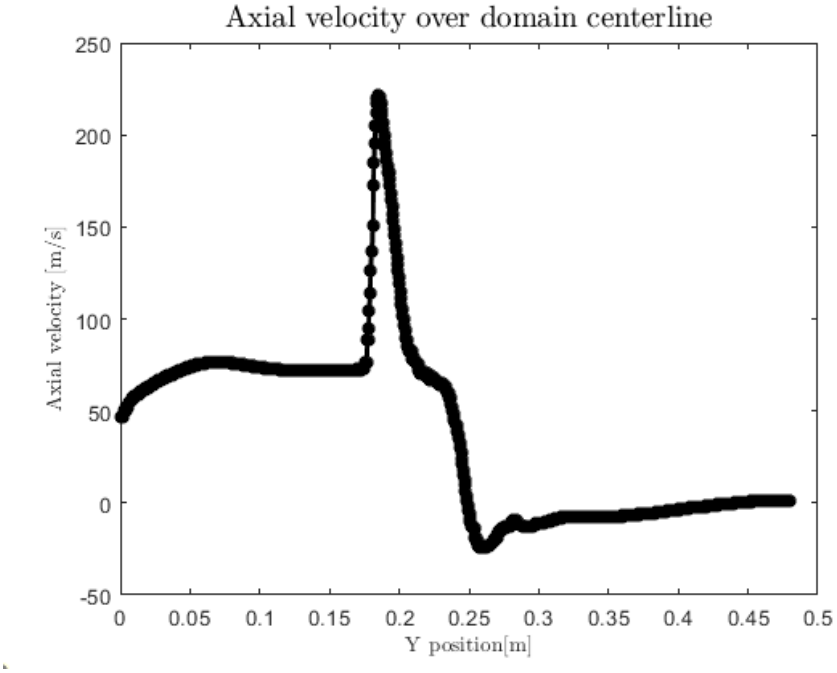

Figure 4.25: Axial velocity over domain centerline (Y axis)

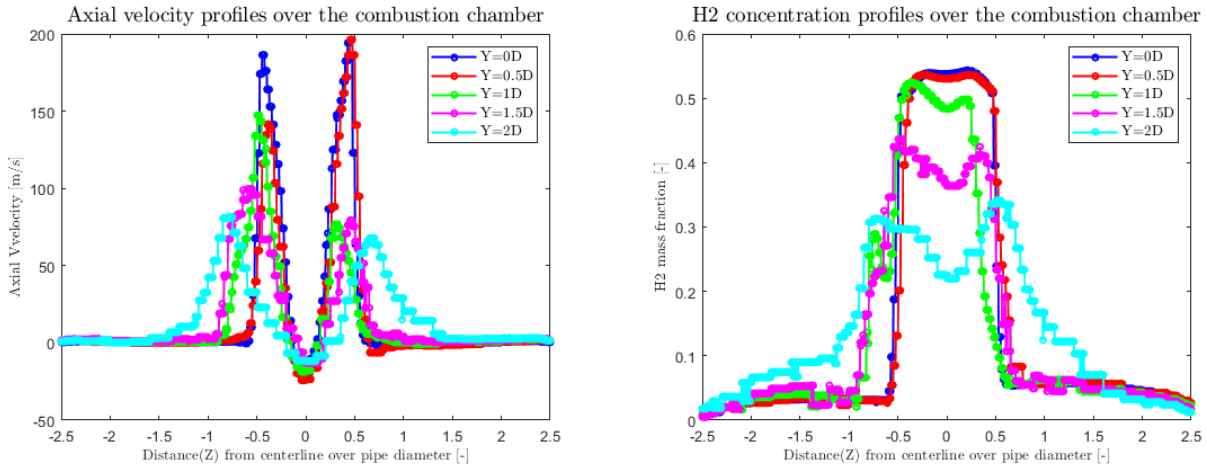

Figure 4.26: Velocity and mass fraction profiles over the dimensionless distance at probing lines

In order to have an idea of the physical distribution of the species, in Figure 4.27, it can be

appreciated the previously developed idea about the locations of thechamber which are closer to the inlet not having a wide distribution of hydrogen. This issue is caused because the injection velocity is too high, so the radial expansion of the jet coming from the pipe is not fast enough to match the small time scales on which the axial jet advances. This is, in the place where the pipe finishes, those sharp corners generate a zone where hydrogen concentration will not be high enoguh, therefore wasting space in the chamber.

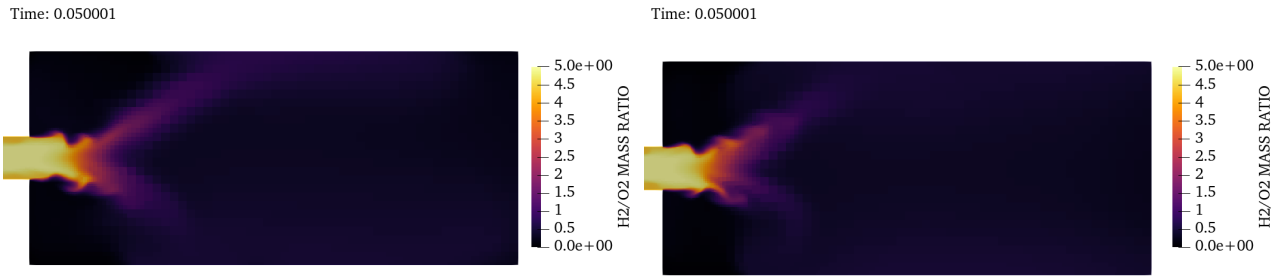

Figure 4.27: Hydrogen mass over oxygen mass ratio contour

4.1.5 Case 5

In the last case simulated, the hydrogen mass fraction sits between the one used in case 4 and case 3 for the outer inlet, while the inner inlet is maintained to be 100 % hydrogen. In this case, the behavior is also intermediate between case 3 and case 4 for the flow entering the combustion chamber. This is, the swirling motion has some effect on the flow, but it is not the only phenomenon driving the gas conduct. Proof of this is the fact that the zone where high velocity magnitudes are observed is narrower in both slice planes in Figure 4.28.

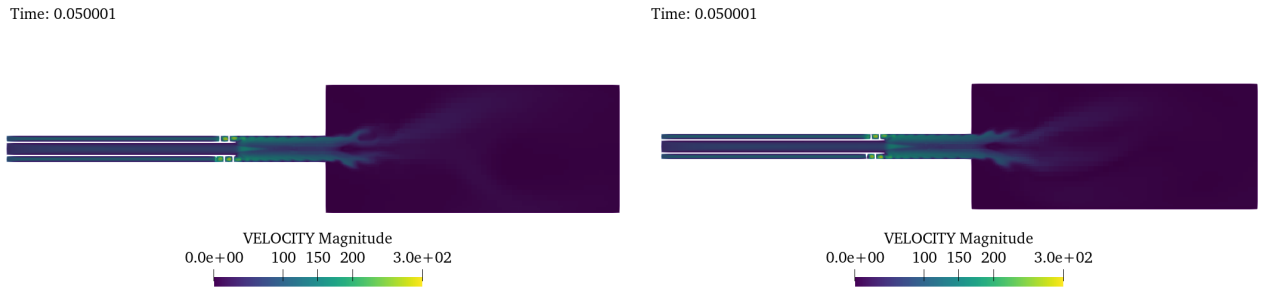

Figure 4.28: Velocity contours on X-plane (left) and Z-plane (right) slices of the geometry

When looking at the results from the probing points (Figure 4.29), it can be noted that the IRZ is created, because of the negative values of the Y-velocity (axial) component at points 2 and 4. As in previous cases, the non-axial components have some fluctuations around 0 for these points because of the excentricity and non-symmetry of vortex breakdown structures inside de chamber, but in this particular case, the properties of this cyclic behavior are much less noticeable. Reinforcing the idea that the flow is somewhere between the two cases analyzed above, the velocity values at point 5 are very chaotic and do not stabilize over time. This is because the flow is a mixture between a jet and a swirling flow and therefore the vortex breakdown structures are formed later in the combustion chamber. Also due to this fact, point 3 has been skipped in the graphs because it is not strongly influenced by the flow because of its position, too far from the centerline and near the combustion chamber inlet, similarly as it happens in case 4.

The early peak in axial velocity and velocity magnitude, which has also been seen in the results from other cases, is due to the gas coming from the outer inlet (the one in charge of

slowing down in the axial direction the flow by introducing movement in other directions), takes some more time to reach the combustion chamber because of having to go through the swirler geometry compared to the air on the inner inlet, which carries less mommtum, but this is rapidly corrected when the swirling starts affecting the flow. This explains why in cases 2 and 3, where the swirling has less influence on the flow, this peak is not so noticeable as in this case for example.

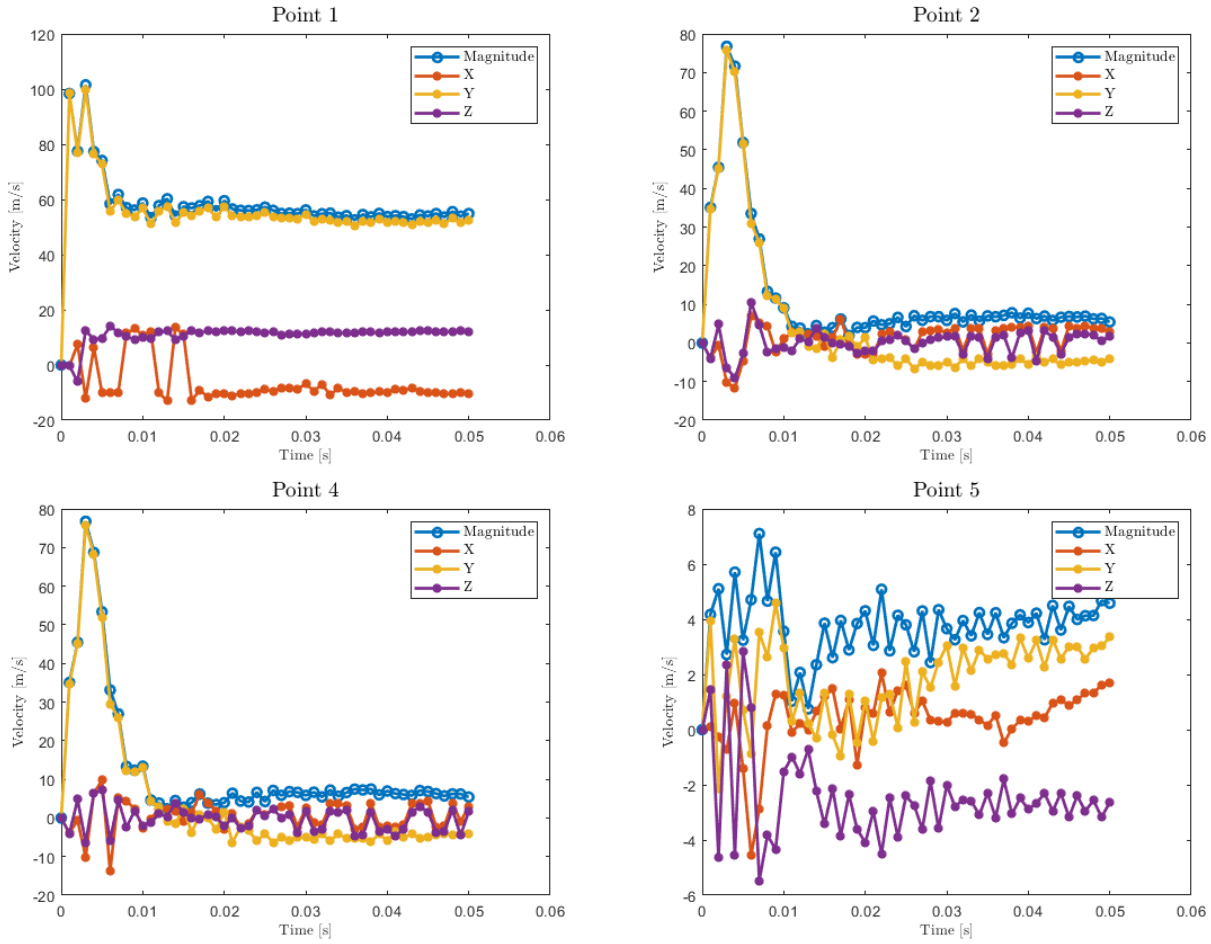

Figure 4.29: Velocity at points 1, 2, 4, and 5 over time

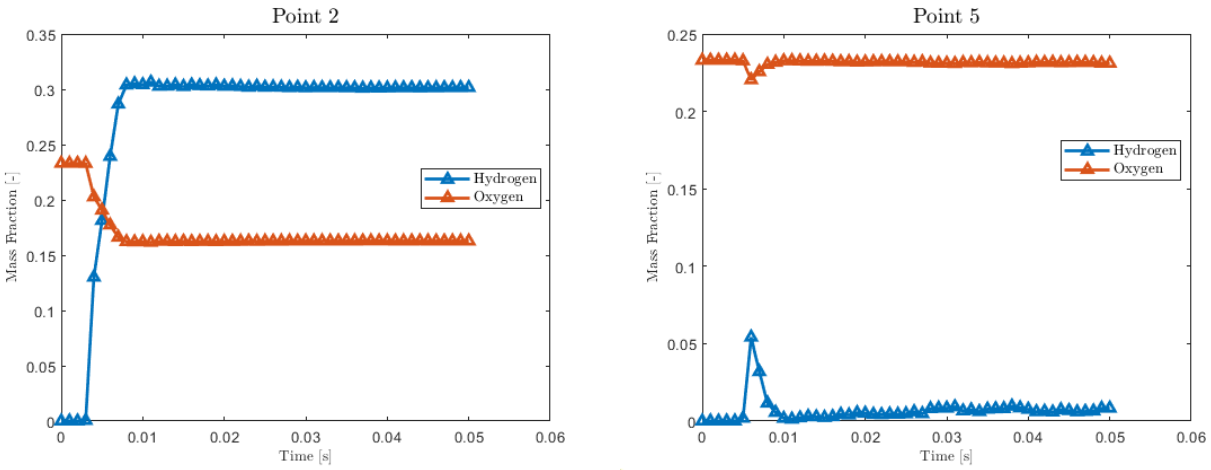

Figure 4.30: Mass fraction at point 2 and point 5 over time

The narrowing of the swirling tube in the combustion chamber has a negative impact on fuel

distribution (Figure 4.30), making the point far from the centerline not to have any hydrogen concentration or making it negligible. The instability of the flow may cause, at some specific time, the flow asymmetries to provoke a temporary change in velocity distribution which brings some more fuel to these points, but this may also cause flame inestability problems and uneven combustion.

When looking at the axial velocity distribution along the domain´s centerline (Figure 4.31), it can be observed that the length of the IRZ is much lower than in previous cases, because the axial velocity rapidly bounces back to a positive value. However, it seems that then it comes again back to near-zero values, this might suggest that the recirculation in the centerline of the combustion chamber happens twice.

In addition to this, when taking a closer look at the part of the graph between 0.2 m and 0.25 m of Y direction distance, it can be noticed that after the outer stream introduces a high velocity in the flow, the velocity falls down to roughly the same value again and then slightly accelerates just before entering the combustion chamber. This is the only case where this happens, and it could be caused by the fact that the inner inlet velocity has a bigger weight in the system´s behavior, and therefore is able to add some momentum to the flow that has been slowed down by the swirling motion. This fits with the theory that the main feature that differentiates this case from the others is that the flow enters the combustion chamber with a higher axial momentum ratio over the momentum in radial and tangential directions.

By taking a look at the velocity vectors in the combustion chamber (Figure 4.32), it can be seen the difference between this case and the ideal performance of the system (Figure 4.9). Here there are for sure some recirculations, but they seem to be more random fluctuations on the jet development than a proper IRZ, also there is no CRZ at all, which might explain the results of poor stabilization in the early stages of the chamber and outside the centerline (Point 5 in Figure 4.29).

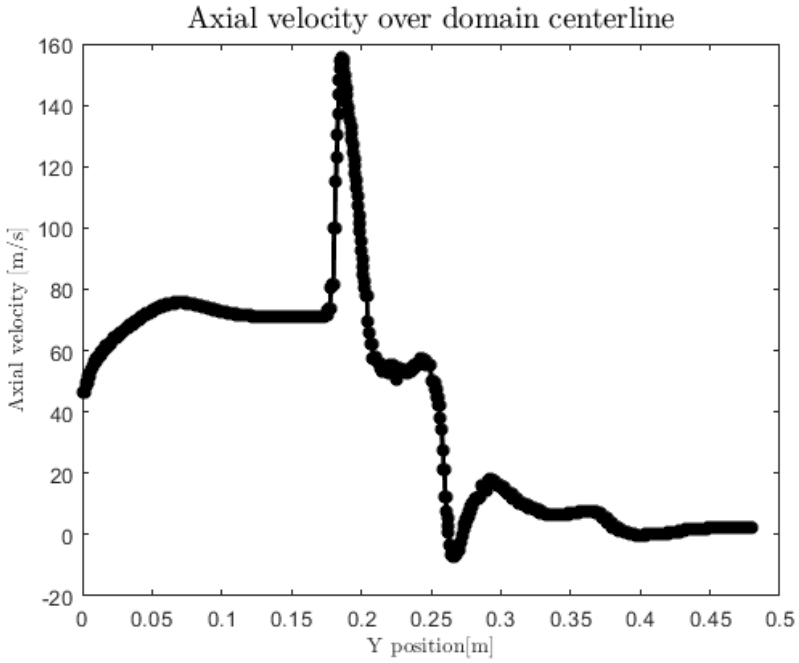

Figure 4.31: Axial velocity over domain centerline (Y axis)

Finally, the profiles both of axial velocity and mass fractions on the probing lines (Figure 4.33) perfectly capture this intermediate behavior between cases 2 and 4, where the “M” shaped velocity profile is present in the earlier lines, but then starts to deform due to these recirculation zones formed in the combustion chamber. The non-swirling inner stream also has an influence

on the profiles not to exhibit high asymmetries in the "M" shapes as in previous cases. Regarding the hydrogen mass fraction distribution, the swirling motion is not strong enough in this case to make this profiles "M" shaped as well. In fact, this is the only case where the area containing an important quantity of hydrogen gets narrower as the flow advances inside the chamber. Again, the rounded shape that the mass fraction profiles acquire is halfway between the sharp profiles from case 2 and the flatter distribution present at the center part of the mass fraction profiles at case 1 for example.

One of these "random" recirculation zones can be seen in the velocity profile for line 4, where the profile has an extra peak apart from the two expected, this can happen if the swirling profile gets affected by a high radial pressure gradient which is caused by the high axial speed in the jet tube, and can eventually displace this zone with higher tangential velocities.

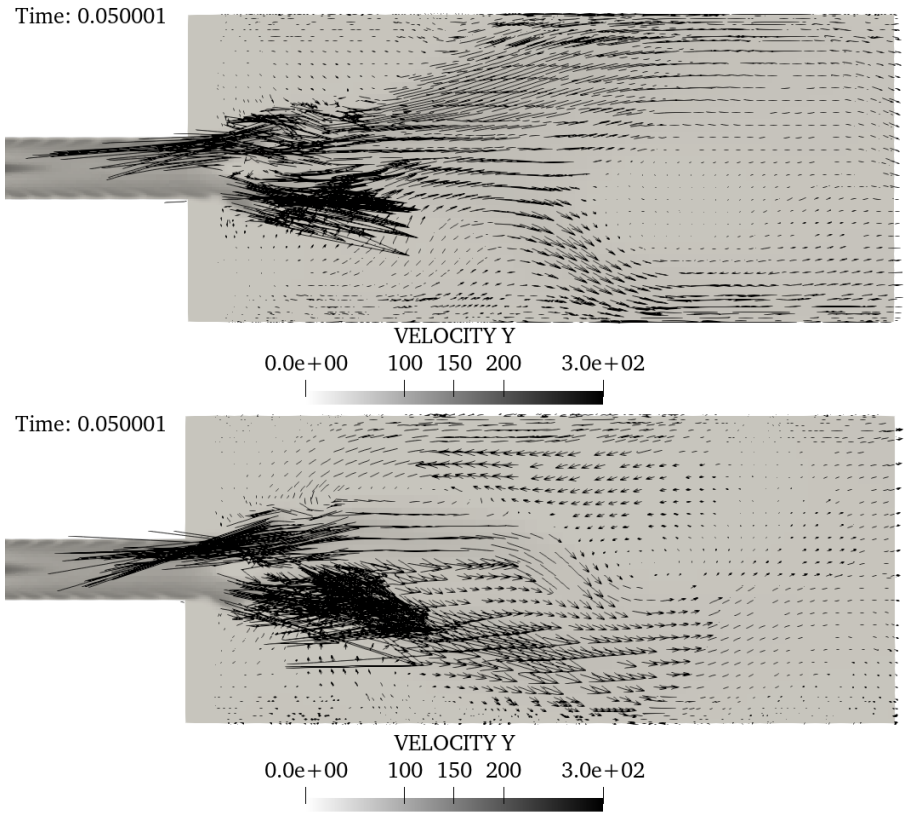

Figure 4.32: Plane X (top) and Z (bottom) slices with velocity vectors

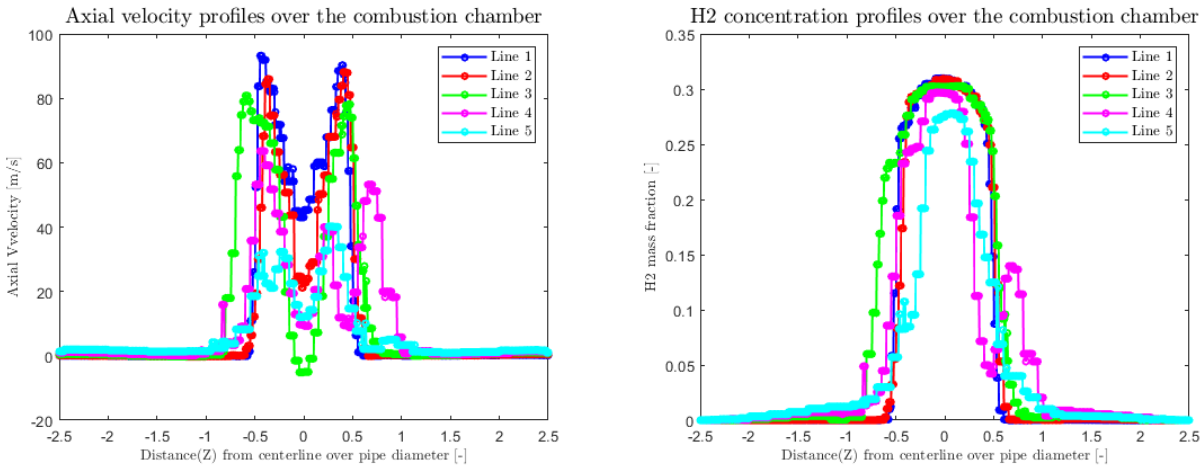

Figure 4.33: Velocity and mass fraction profiles over the dimensionless distance at probing lines

4.2. LES Results and comparison

As shown in Figure 4.1, the LES simulation was carried out using a 50 % Hydrogen mass fraction on both the outer and the inner inlet. Therefore, when looking at the results of this case, it might be useful to revisit Section 4.1.1, which was done with exactly the same boundary conditions. The LES approach is supposed to produce results that differ notably from RANS simulations, primarily in their portrayal of turbulent flow. In LES, the focus lies on directly resolving larger turbulent structures while modeling the smaller ones, providing a more detailed and unfiltered view of turbulence. Thus, the anticipated differences between LES and RANS results primarily stem from the level of detail and accuracy in depicting turbulent phenomena within the simulated flow field.

The very first result exposed, already makes clear the difference between both approaches. The smooth field that was present in velocity contours for the RANS simulation (Figure 4.5) gives way to a much more chaotic appearance for the LES case, where instead of the large "bubbles" of the domain where high velocity happens in a certain range of time, now the contour looks much more like the actual flow on the domain in a given moment on time (Figure 4.34). Even some of the bigger eddies resolved by the equations can be spotted when looking closely to the combustion chamber inlet (Figure 4.35).

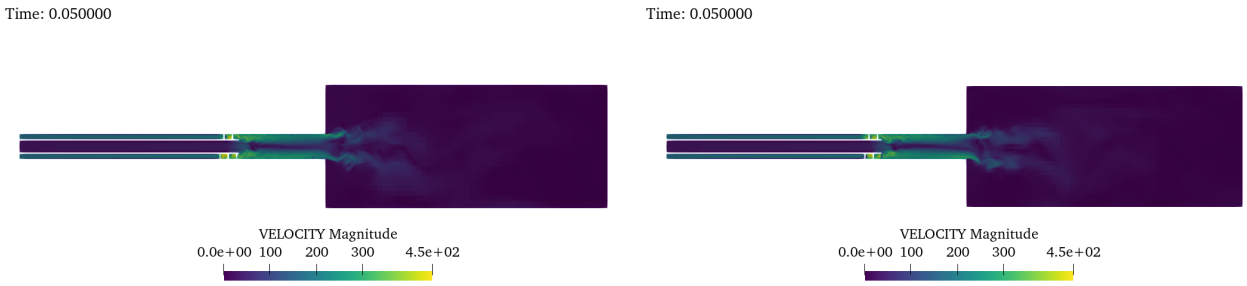

Figure 4.34: Velocity contours on X-plane (left) and Z-plane (right) slices of the geometry

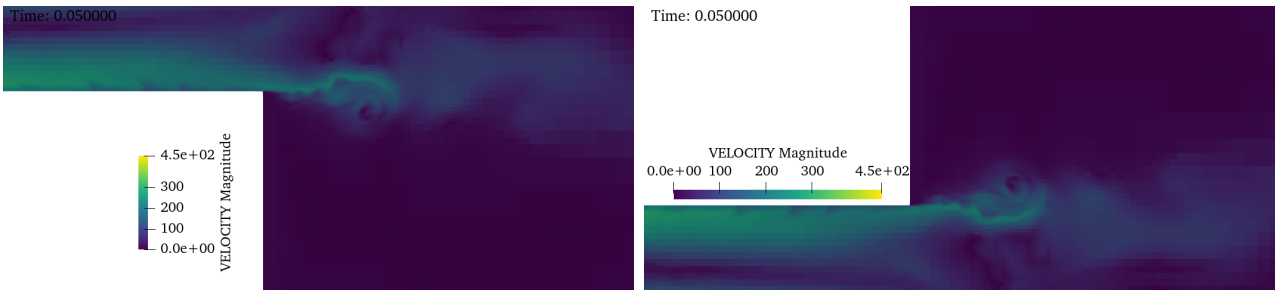

Figure 4.35: Closer looks on the X-plane and Z-plane slices at the entrance of the chamber

Moving onto the probing points analysis, the very first thing that differs from the results obtained using RANS modeling is that there is a very important difference in magnitudes for the three velocity components, this difference can be up to 100 % of the actual value.

First, in the points that are closer to the inlet and in the centerline (Points 1 and 2), the velocity magnitude is much higher for the LES simulation. This is probably caused by the higher values that the non-axial components of velocity (namely X and Z) have. Thus, the periodic behavior of those components on point one that was already noticed, gains amplitude as the LES might be capturing the whole importance of these fast fluctuations. By using the FFT, the main frequencies of both the X and Z components of velocity can be spotted (Figure 4.36).

The similarity in the peak frequencies of both components means that the behavior in both main radial directions is the same, not being highly affected by the non-axisymmetric shape of the combustion chamber. Both components have smaller peak frequencies at around 60 Hz and 200 Hz, this second one would mean a period of 0.005 s, which may correspond to the earlier stages of the simulation where the fluctuations are faster and have less amplitude. Finally, the main peak is around 120 Hz, which would mean a slightly bigger period and is associated with posterior stages of the simulation where the non-axial velocity fluctuations are less noisy and start being slower.

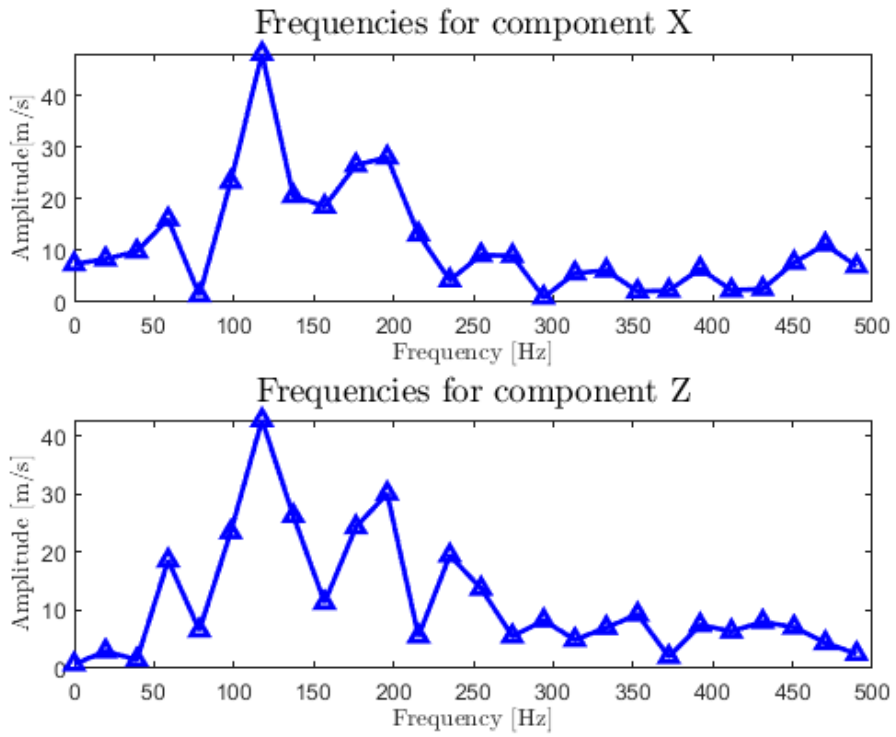

Figure 4.36: Frequency analysis for X and Z components of velocity at point 1

Secondly, for the points outside the centerline, the values of all three cartesian components of velocity are bigger for the LES simulation near the inlet (Point 3) whereas the RANS values seem to be slightly bigger for Point 5, which is further away from it. In this case, the results for the different approaches relatively maintain the same shape as in the RANS case, showing oscillations that do not have a strong periodic behavior, or not fast enough to be captured during the length of the simulation.

Lastly, for Point 4, the farthest away point of the combustion chamber inlet, the reported velocities are similar to the ones obtained modeling all the turbulence in the domain, except for the axial component of velocity, which seemed to be negative at all times once the case stabilized in the RANS results, while in the current results, the axial component of velocity does not seem to be maintained on negative values on the whole second part of the simulation, but instead fluctuates between positive and negative values. This fact has for sure a big influence on the stability, shape, and even existence of the IRZ.

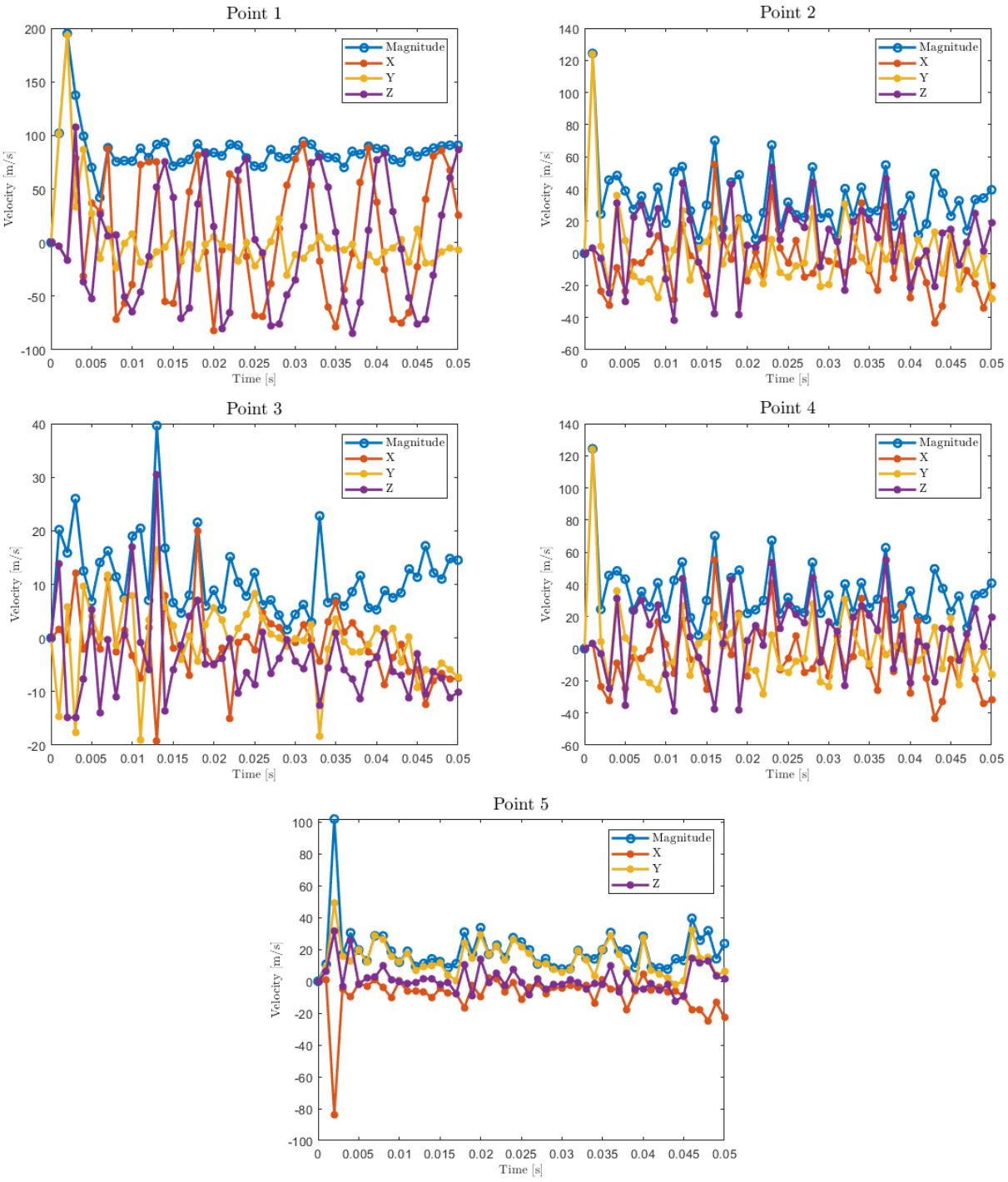

Figure 4.37: Velocity at points 1, 2, 3, 4, and 5 over time

These differences in the velocity values contrast with the mass fraction results, where, except for the LES case being less stable, especially around the places where the IRZ should be created (Points 2 and 4), the results from both simulations are nearly identical. This could mean that the differences in velocity values mentioned above are just a result of the LES capturing more of the turbulent behavior of the flow, and therefore having a fluctuating velocity profile, but those small fluctuations do not affect the species transport enough to see important differences when looking at overall results.

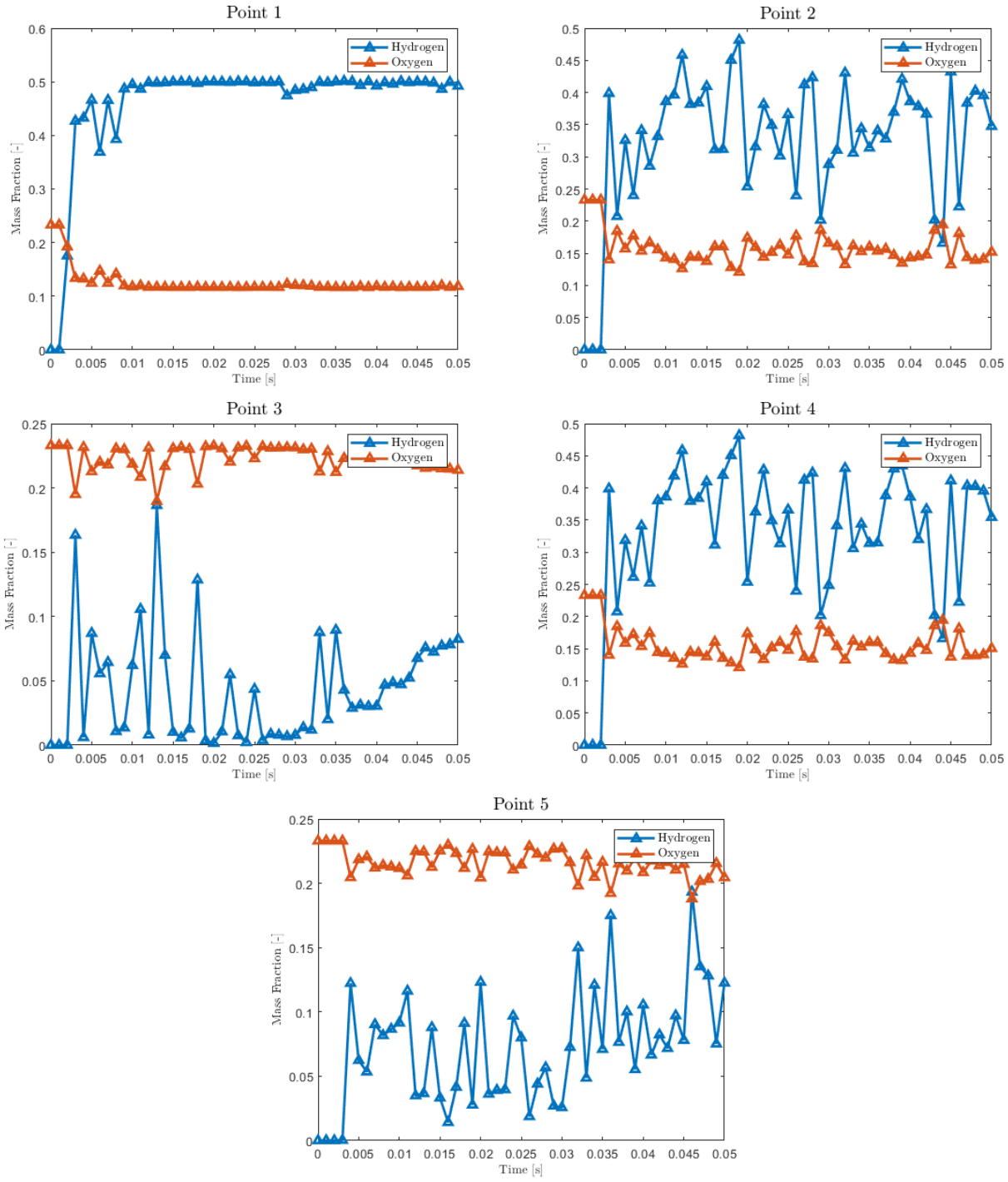

Figure 4.38: Mass fraction at points 1, 2, 3, 4, and 5 over time

The results from the velocity points could lead to the thought that the IRZ is not formed when resolving the case with LES turbulence modeling. However, when seeing the axial velocity profile over the centerline (Figure 4.39), the drop in the axial velocity when entering the combustion chamber is still there. Despite these initial values, it has a rebound effect and the negative velocities do not last up until the end of the combustion chamber as they do in the results of the RANS approach.

Apart from that, there seems to be an additional recirculation point when the flow is still inside the common inlet pipe, which remained completely unseen in RANS, this is most certainly due to the big velocity difference between both streams coming from the different inlets, and in the mixing moment the radial components induced by the swirlers, make the outside pipe flow, which carries much more momentum than the inside one, create this small recirculation

point.

The graph has in this case bigger difference between peak values and sharper fluctuations, as might be expected.

When looking at the velocity vectors for this case, Figure 4.40 (specially the Z slice) summarizes one of the key insights of the LES results. The IRZ and CRZ loose size and importance in favor of some other spontaneous recirculation zones created along the chamber. It must be taken into account that this image cannot be directly compared to the RANS simulation, as a temporal averaging would be needed to do so.

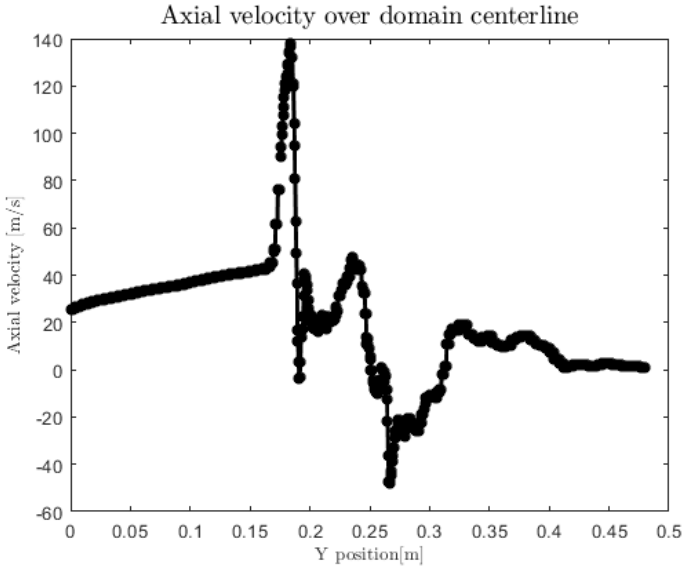

Figure 4.39: Axial velocity over domain centerline (Y axis)

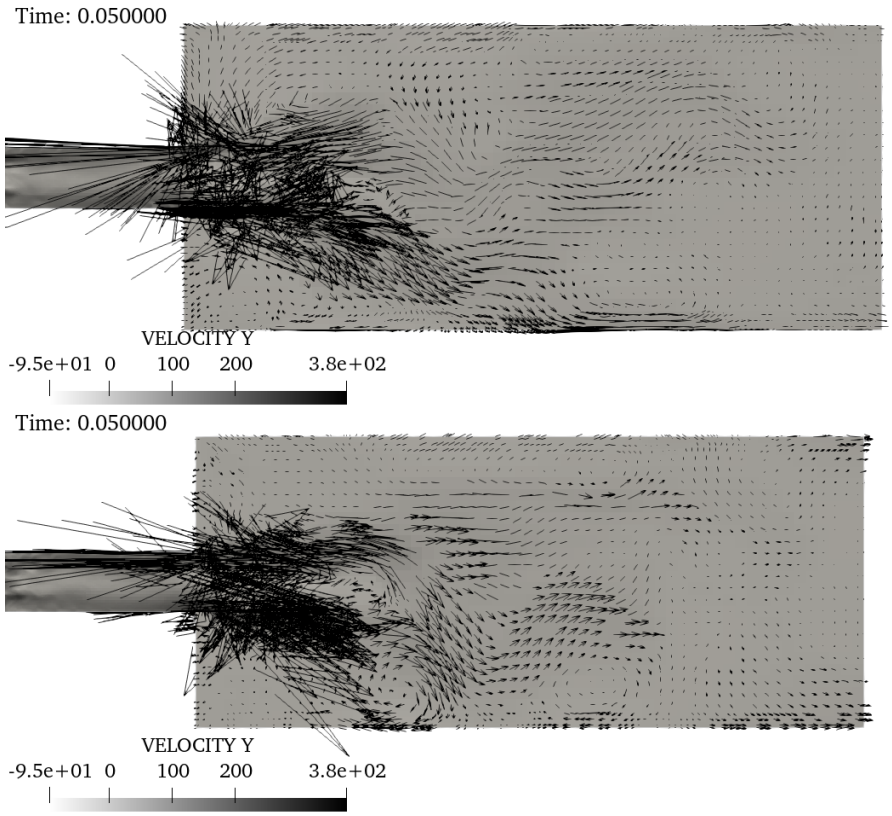

Figure 4.40: Plane X (top) and Z (bottom) slices with velocity vectors

Regarding the velocity and mass fraction distribution in the probing lines, two pairs of graphs have been created:

- In Figure 4.41, the plotted values have been circumferentially averaged, so as not to allow any local fluctuation to influence the results. In the velocity profile graph, the "M" shape is only maintained through the first three lines, which means the large turbulent structures inside the chamber are short, making the flow´s behavior inside the chamber change from the desired result, where the IRZ provides a correct mixing of the fuel and the oxidizer and also controls the axial velocity not to be too high, to a much more chaotic scenario where there is a front of axial velocity advancing inside the combustion chamber. This will substantially reduce the performance of the turbine. On the mass fraction side, the result is equally worrying, as this vortex breakup seems to be strong enough to create an even distribution of hydrogen through the chamber. However, this is the parameter that will be more influenced when combustion is added to the calculations, so this might only be a partial win.

- On the other hand, the graph in Figure 4.42 has been created with only one line, as the ones reported for the RANS cases, having these allows us to focus on the main differences between this graph and the one in Figure 4.13, where, apart from the tendency to have slightly higher velocities in the LES results, there no big differences between both approaches except for one. The velocity results in the LES case have some spots where the axial velocity is negative even though those points are not located near the centerline. This is in harmony with the higher velocities, and the smaller zone where there is a negative axial velocity in the centerline in the LES results, essentially, all this sums up in that when using the LES approach, the IRZ is predicted to be less dominant over the behavior of the flow inside the combustion chamber. Regarding the hydrogen mass fraction profiles, another important difference can be observed in the fact that the hydrogen mass fraction profile is flat around the centerline for the RANS case, while for the LES results the "M" shape starts much sooner and also vanishes more quickly. This could be caused by the turbulence model itself or also by the discretization error introduced when choosing the mesh size.

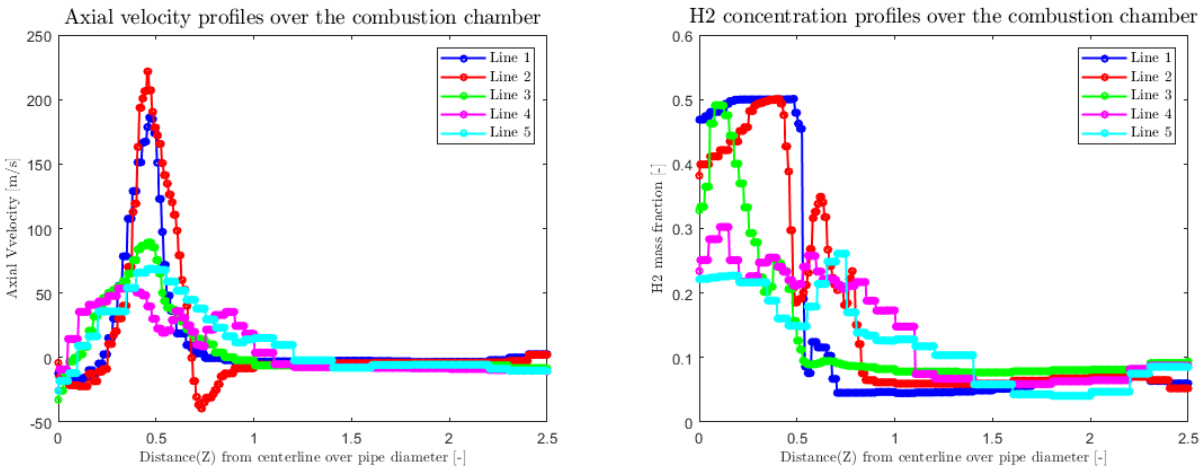

Figure 4.41: Circumferentially averaged velocity and mass fraction profiles over the dimensionless distance at probing lines

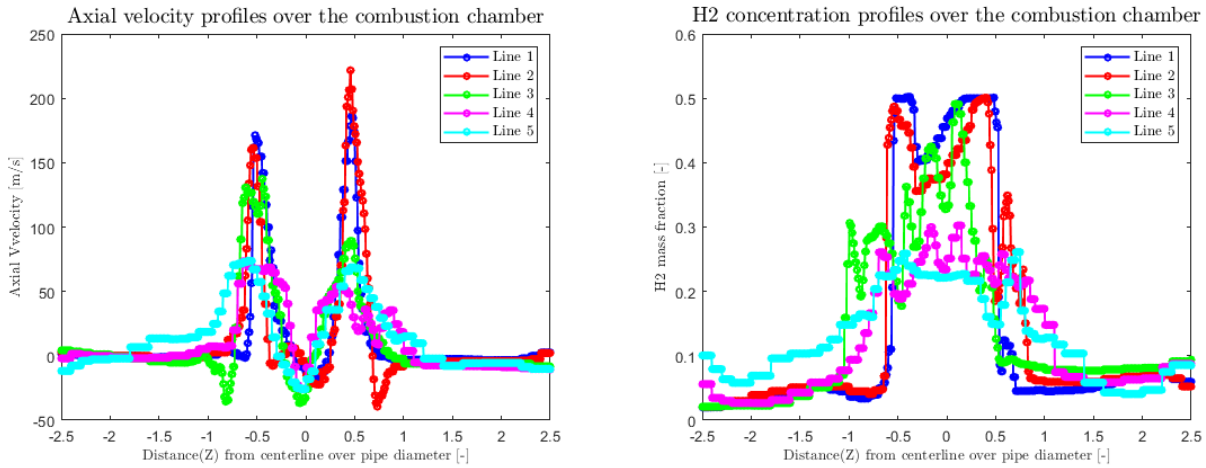

Figure 4.42: Velocity and mass fraction profiles over the dimensionless distance at probing lines

In Figure 4.43, the H_2 to O_2 mass fraction ratio shows how these velocity fluctuations do affect the species concentration inside the chamber, as both the X and Z slices show important asymmetric behavior. However, this ratio is highly influenced by the cold flow simulation assumption, where the combustion was not modeled, so the actual functioning of the burner has probably a lot of differences with this case.

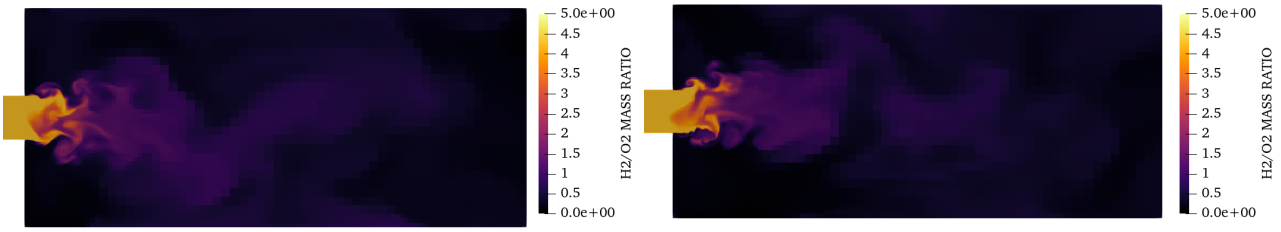

Figure 4.43: Hydrogen over oxygen mass ratio contour on X (left) and Y (right) plane slices

5. Concluding remarks

5.1. Main conclssions

The analysis carried out in this thesis, while being highly biased by the imposed assumptions on the model in the first place, has drawns some conclusions worth mentinoning. The main objectives of the project have been fullfilled, as the turbulent structures created by the so-called "swirlers" have been identified and their differences analyzed for multiple parameter combinations. The most important conclusions which can be extracted from this work about the operation of aeronautical combustion chambers running on hydrogen as a fuel.

1. When operating two-inlet burners where one of the streams is influenced by a swirl-induced geometry, the velocity ratio between both streams will have a huge influence on the behavior of the flow once these two streams are mixed and even on the mixing process. If the non-swirled stream is dominant over the mixing, the result will be a jet-type flow which is not desired because it will harm the performance of the burner. On the other hand, if the swirled stream velocity is too high, this might cause stability problems on the turbulent structures formed in the combustion chamber, moreover, a low velocity in the non-swirled stream will also mean that it is under-used and therefore the performance of the whole device. This was not one of the main objectives of the present work, but has been discovered as a side-consequence of doing large changes in the species composition of the inlet gas, while maintaining the mass flow constant. When moving leftwards in the Inner vs Outer inlets hydrogen mass fraction matrix (Figure 4.1), the cited effect of the jet-type behavior becomes dominant and spoils the chambers performance.

2. The formation of the two main turbulent structures inside the combustion chamber (IRZ and CRZ) is crucial to ensure the correct functioning of the system. From the velocity perspective, it has been proven that the formation of these structures creates a suitable environment for the sustained operation of the burner, preventing problems like the flame blow-off. Besides, from the fuel and oxidizer concentration perspective, these structures allow the improvement of the burner as a whole, making the most of the available space, as the more homogeneous the fuel-to-oxidizer ratio is, the more space is actually being used for combustion in the desired fuel richness range. This will allow the device's dimensions to be smaller, which is a crucial parameter when designing aeronautical engines.

3. The velocity magnitude differences between the results obtained for the same case using RANS and LES methods are concerning. While spatial discretization-related issues might have some influence on those, the differences are too large to be only blamed on that and this might mean that the RANS approach is not enough to capture the unsteady processes happening on the flow. This statement will be backed by the current industry standards where RANS simulations do not play an important role in aeronautic combustion chamber CFD calculations [14].

4. The small-scale high-frequency velocity fluctuations present only when using the LES approach, do not correlate to important differences in the species concentration but might have a huge impact on the system performance when including combustion modeling into the calculations, as the chemical time-scales, much smaller than the convective transport timescales for fuel oxidation [3].

5. Regarding the case setup, while this setup can be used as a template for developing a more sophisticated workflow on hydrogen burner simulation, some modifications are advised in the next chapter. Furthermore, a closer look on diffusion and its effects is also advised but its outside the scope of this project.

5.2. Future work

Once the main goals of the project are fulfilled, some other avenues of development have been found in order to improve the understanding of the device and its modeling:

- The very first topic to address when going on with this project is to define more accurately the mass flow paramteres in both inlets which ensure the flame stability and turbulent structures formation.

- Furthermore, including combustion modeling into the simulation will give a wider picture of the actual operation of the combustion chamber, and most surely affect the flow behavior in a two-way interaction which will help to optimize the input parameters for the performance of the system.

- While the RANS results are taken as good for the sake of this thesis, it is necessary for this project to be trustable that the mesh is changed to the point where the mesh independence is achieved. For the LES simulation, the results for the mesh quality assessment were certainly better, but to be consistent with the formulation of the equations there is also some work to do with the mesh. Carrying on the project using sub-optimal meshes was a decision made taking into account the amount of time aimed for the project and the available resources. For both RANS and LES meshes, the way to go in order to get better spatial discretizations would be to go higher on the maximum number of cells

- Going longer on the total amount of simulation time will for sure be helpful in the support of some of the concussions in this project, especially in the velocity fluctuation characterization for the non-axial components in the centerline of the combustion chamber, as the evolution of the period of those fluctuations was on a growing trend in the last data points.

- The number of combinations of the two modified parameters was good enough to qualitatively state where the operating point should be, but this is a very coarse result that could be enhanced with the simulation of 5-10 more parameter sets. In between the cases where the behavior of the flow is on the desired trend, small changes in the inflow species mass fractions could be used together with statistical methods to get a narrower range where the performance of the chamber is optimized.

6. Bibliography

[1] Airbus. Hydrogen: An important decarbonisation pathway, 2023. URL https://www.airbus.com/en/innovation/low-carbon-aviation/hydrogen.

[2] P. Anacleto, E. C. Fernandes, M. V. Heitor, and S. I. Shtork. Swirl flow structure and flame characteristics in a model lean premixed combustor. *Combustion Science and Technology*, 175(8):1369–1388, 2003.

[3] M. D. Barre. *Simulation Numerique de l'alumage dans les chambres de combustion aeronautiques*. PhD thesis, Insitut National Polytechnique de Tolouse, 2014.

[4] A. C. Benim and K. Syed. *Flashback Mechanisms in Lean Premixed Gas Turbine Combustion*. 01 2015. ISBN 978-0-12-800755-6.

[5] I. Celik, Z. N. Cehreli, and I. Yavuz. Index of resolution quality for large eddy simulations. *Journal of Fluids Engineering*, 127:949–958, 2005.

[6] I. Celik, M. Klein, and J. Janicka. Assessment measures for engineering les applications. *Journal of Fluids Engineering*, 131, 2009.

[7] B. L. Center. Nitrogen oxides, 2023. URL https://www.babcock.com/home/about/resources/learning-center/nitrogen-oxides-nox-primer.

[8] H. Council. Hydrogen council main page, 2023. URL https://hydrogencouncil.com/en/.

[9] R. Courant, K. Friedrichs, and H. Lewy. Über die partiellen differenzengleichungen der mathematischen physik. *Mathematische Annalen*, 100:32–74, 1928.

[10] R. Domingues, F. Brójo, and P. Oliveira. Cfd analysis of the combustion of hydrogen fuel on a cfm56-3 combustor. *ASME 2022 International Mechanical Engineering Congress and ExpositionASME 2022 International Mechanical Engineering Congress and Exposition*, 2022.

[11] E. C. for Climate Action. Reducing emissions from aviation, 2021. URL https://climate.ec.europa.eu/eu-action/transport-emissions/reducing-emissions-aviation_en.

[12] A. Gerasimov. Quick guide to setting up les-type simulations. ANSYS Customer Portal, 2016.

[13] M. German, U. Piomelli, P. Moin, and C. W. H. A dynamic subgrid-scale eddy viscosity model. *Physics Fluids A.*, 1991.

[14] L. Gicquel, G. Staffelbach, and T. Poinsot. Swirl flow structure and flame characteristics in a model lean premixed combustor. *Progress in energy and combustion*, 38:782–817, 2012.

[15] G. Kalitzin, G. Medic, G. Iaccarino, and P. Durbin. Near-wall behavior of rans turbulence models and implications for wall functions. *Journal of Computational Physics*, 204:265–291, 2005.

[16] T. Kalm'ar-Nagy and B. D. Bak. Reproducing the kolmogorov spectrum of turbulence with a hierarchical linear cascade model. *arXiv: Chaotic Dynamics*, 2018.

[17] K. G. Kyprianidis. *Advances in Gas Turbine Technology*, chapter Future Aero Engine Designs: An Evolving Vision. IntechOpen, 2015.

[18] C. Levingston. Ge aviation's roadmap for the future of flight, 2022. URL https://blog.geaerospace.com/sustainability/ge-aviations-roadmap-for-the-future-of-flight/.

[19] A. C. Lewis. Optimising air quality co-benefits in a hydrogen economy: a case for hydrogen-specific standards for nox emissions. *Enviromental Science: Atmospheres*, 1:201–207, 2021.

[20] A. C. Lewis. Optimising air quality co-benefits in a hydrogen economy: a case for hydrogen-specific standards for nox emissions. *Enviromental Science: Atmospheres*, 201(1):201–207, 2021.

[21] O. Lucca-Negro and T. O'Doherty. Vortex breakdown: a review. *Progress in Energy and Combustion Science*, 27(4):431–481, 2001.

[22] MazdaNewsroom. Mazda starts leasing rotary hydrogen vehicles, 2015. URL https://newsroom.mazda.com/en/publicity/release/2006/200602/060215.html.

[23] J. Nagao. Numerical investigation of wall effects on combustion noise from a lean-premixed hydrogen/air low-swirl flamenumerical investigation of wall effects on combustion noise from a lean-premixed hydrogen/air low-swirl flame. *Physics of fluids*, 35(1), 2023.

[24] NASA. Properties of air, 2023. URL https://www1.grc.nasa.gov/beginners-guide-to-aeronautics/properties-of-air/.

[25] D. Pashchenko. Comparative analysis of hydrogen/air combustion cfd-modeling for 3d and 2d computational domain of micro-cylindrical combustor. *International Journal of Hydrogen Energy*, 42(49):29545–29556, 2017.

[26] S. B. Pope. *Turbulent Flows*. Cambridge university press, 2000.

[27] PrattWhittney. Gtf engine: Roadmap to the future, 2023. URL https://www.prattwhitney.com/en/newsroom/news/2023/06/19/gtf-engine---roadmap-to-the-future.

[28] RollsRoyce. Pioneering intelligent innovation for our customers, 2023. URL https://www.rolls-royce.com/products-and-services/civil-aerospace/future-products.aspx#/.

[29] H. Schlichting and K. Gersten. *Boundary-Layer Theory*. Springer, 2017.

[30] C. Science. Converge manual.

[31] Z. Shang, J. Lou, and H. Li. Cfd of dilute gas–solid two-phase flow using lagrangian algebraic slip mixture model. *Powder Technology*, 266:120–128, 2014.

[32] C. Soares. *A Handbook Of Air, Land And Sea Applications*. Butterworth-Heinemann, 2012.

[33] L. Tay-Wo-Chong, M. Zellhuber, T. Komarek, H. Im, and W. Polifke. Combined influence of strain and heat loss on turbulent premixed flame stabilization. *Flow Turbul. Combust.*, pages 1–32, 01 2015.

[34] S. Toosi and J. Larsson. Towards systematic grid selection in les: Identifying the optimal spatial resolution by minimizing the solution sensitivity. *Computers and fluids*, 201, 2020.

[35] ToyotaGazooRacing. Toyota gazoo racing unveils 'gr h2 racing concept' at le mans 24 hours, 2023. URL `https://toyotagazooracing.com/wec/release/2023/0609-01/`.

[36] S. Verhelst and T. Wallner. Hydrogen-fueled internal combustion engines. *Progress in Energy and Combustion Science*, 35:286–295, 2009.

[37] H. Wemer and H. Wengle. Large-eddy simulation of turbulent flow over and around a cube in a plate channel. 1993.

[38] F. A. Williams. Detailed and reduced chemistry for hydrogen autoignition. *Journal of Loss Prevention in the Process Industries*, 21:131–135, 2008.

[39] V. Yakhot, S. Thangam, T. B. Gatski, S. A. Orszag, and C. G. Speziale. Development of turbulence models for shear flows by a double expansion technique. *Physics of Fluids A Fluid Dynamics*, 1992.

7. Annex I: Mathematical definitions

Dirichlet and Neumann Boundary conditions

Dirichlet

The Dirichlet boundary conditions state the value that the solution function f to the differential equation must have on the boundary of the domain C.

$$f(x,y) = g(x,y,...) \; where \; x,y \in \partial C$$

Neumann

The Neumann boundary conditions state that the derivative of the solution function f to the differential equation must have a given value on the boundary of the domain C.

$$\frac{\partial f(x,y)}{\partial x} = g(x,y,...) \; where \; x,y \in \partial C$$

or

$$\frac{\partial f(x,y)}{\partial y} = g(x,y,...) \; where \; x,y \in \partial C$$